UNIVERSITY OF OKLAHOMA

GRADUATE COLLEGE

HYDRAULICALLY-INDUCED MICROSEISMIC FRACTURE CHARACTERIZATION FROM SURFACE SEISMIC ATTRIBUTES AND SEISMIC INVERSION: A NORTH TEXAS BARNETT SHALE CASE STUDY

A THESIS

SUBMITTED TO THE GRADUATE COLLEGE

In partial fulfillment of the requirements for the

Degree of

MASTER OF SCIENCE

By

XAVIER EDUARDO REFUNJOL CHIRINOS

Norman, Oklahoma

2010

HYDRAULICALLY-INDUCED
MICROSEISMIC FRACTURE CHARACTERIZATION
FROM SURFACE SEISMIC ATTRIBUTES AND SEISMIC INVERSION:
A NORTH TEXAS BARNETT SHALE CASE STUDY

A THESIS APPROVED FOR THE
CONOCOPHILLIPS SCHOOL OF GEOLOGY AND GEOPHYSICS

BY

____
Dr. Katie M. Keranen

____
Dr. Kurt J. Marfurt

____
Dr. Joel H. Le Calvez

____
Dr. Deepak Devegowda

____
Dr. Larry R. Grillot

For my mother and father, on whose shoulders I stood as the waters rose high.

May my shoulders be as tall for mine.

ACKNOWLEDGEMENTS

I would like to express my gratitude to all those who have encouraged and assisted me in during this project. Special thanks to my advisor Katie M. Keranen, and committee members Dr. Kurt J. Marfurt, Dr. Joël H. Le Calvez, Dr. Deepak Devegowda, and Dr. Larry Grillot for their guidance and continuous input beyond their areas of expertise. I would also like to thank my friends and colleagues for their endless support. To Aliya Urazimanova for being a constant source of motivation and inspiration, and never turning down an extensive theoretical discussion. The faculty and staff of the University of Oklahoma for creating a home away from home. Similarly I would like to thank Devon Energy for sharing their insight, and providing financial support and data for this investigation. Schlumberger and Hampson-Russell have to be acknowledged as well for providing licenses for software used in interpretation and inversion processes respectively. Lastly I would like to thank my mother Belkis T. Refunjol and father Güynemer A. Refunjol for their unconditional support regardless of the distance, and my sister Giselle A. Refunjol for always being a good influence and setting an example to follow.

TABLE OF CONTENT

LIST OF FIGURES

LIST OF TABLES

1. INTRODUCTION

1.1 Objective

The goal of this project is to predict possible zones of fracture network propagation during hydraulic stimulation by analyzing seismic attributes and acoustic impedance inversion volumes in the North Texas Barnett Shale. The seismic characteristics of the rocks within which the microseismic events cluster serve as characterization and prediction tools for determining weakness and fracture-prone zones from 3D surface seismic acquired before and after hydraulic stimulation. The ultimate objective is to optimize stimulation projects. This minimizes costs necessary to fully produce a reservoir by using an *a priori* estimation of the most likely fracture propagation trends. The area of this case study is within Tarrant County, TX, situated in the eastern edge of the Fort Worth Basin (Figure 1).

1.2 Significance Of Project

The Barnett Shale has proven hydrocarbon resources. The typical measured total organic content (TOC) within the Barnett Shale ranges from 3% and 13% (Loucks and Ruppel, 2007), and the average thermal maturity vitrinite-reflection values (R_o) are between 1.7% and over 2% in gas-prone areas (Jarvie et al., 2007; Martineau, 2007). These values are high enough to make the Barnet Shale a commercially productive play. The Newark East Field within the Fort Worth Basin, located between Wise, Denton and Tarrant County, has estimated mean gas resources of 26 trillion cubic feet (Martineau, 2007; Pollastro et al., 2007). The estimated ultimate recovery from the Barnett Shale is 2.5 – 3.5 billion cubic feet of gas from horizontal wells within core producing areas (Jarvie et al., 2007). However, the Barnett has low porosity (average 6%) and low permeability and is therefore difficult to produce from under natural conditions. Hydraulic stimulation of the formation creates a fracture network that provides a link between the wellbore and hydrocarbons in the porous areas (Jarvie et al., 2007).

The effectiveness of the stimulation program can be evaluated by monitoring hydraulic fractures. Using hydraulic fracture maps we can illustrate drainage pathways generated by pumped fluids. However, thousands of borehole-based microseismic monitoring jobs have shown that expectations as to the hydraulically-induced fracture system development are not always matched by observations. Knowing the current direction of maximum horizontal stress alone does not predict where fractures will occur (Rich et al., 2010). Further, since hydraulic fracture propagation is a time-dependent path of least resistance process, other unaccounted factors can influence rock failure, such as the variability of the local stress field, formation anisotropy, and heterogeneous mineralogical composition. These factors can often result in variable fracture gradients and fracture zones (Jarvie et al., 2007). The variability also increases the risk of fracturing undesirable zones such as water-bearing formations.

To characterize the variations of rock properties within such formations, I generated volumetric curvature volumes (post-stack), as well as seismic inversion volumes (pre-stack) from a 14-square-mile seismic survey targeting the Barnett Shale within the Fort Worth basin using *P*- and *S*-impedance and Lamé parameters from density, shear, and compressional velocity logs acquired in horizontal wells. Having microseismic data recorded before and after the corresponding seismic acquisition presents both the unaltered environment and the resulting fractured setting. I find that the locations of microseismic events correlate to specific values of the inverted surface seismic properties, both in the un-stimulated and stimulated volumes. While volumetric curvature volumes characterize fracture-prone flexures, amplitude inversions products such as acoustic and shear impedance characterize the matrix properties of the Barnett Shale most likely to fail. Further, Lamé parameters shed light on the extent of the fracture system into gas-bearing zones.

Together, surface seismic data and hydraulic fracture monitoring may be used to predict fracture system propagation. Such prediction can have a significant impact on reservoir stimulation planning, risk assessment, and economic evaluation. Accurate prediction and carefully targeted stimulation programs may lead to increased recovery rates through knowledge of possible drainage pathways from target zones.

2. GEOLOGIC BACKGROUND

2.1 Geologic History

The Barnett Shale is the primary source rock for Paleozoic hydrocarbon production in the Bend arch-Fort Worth Basin area (Pollastro et al., 2007). It is a high-thermal-maturity gas-shale system that generates, retains, and stores hydrocarbons (Jarvie et al., 2007). The Fort Worth Basin covers roughly 15,000 mi^2 in north-central Texas, deepens towards the north and its axis roughly parallels the Muenster Arch with a NW-SE trend (Figure 1) (Pollastro et al., 2007). The basin is bounded on the north by the Red River and Muenster Arch basement uplifts. The Mineral Wells Fault crosses the northeastern portion of the basin with a NE-SW trend, similar to the southeastern bounding Ouachita Thrust Fault. The basin becomes deeper in its northeastern portions, where it thickens to 1000 ft, and sediments thin southwest to a few tens of feet (Pollastro et al., 2007).

The Barnett Shale is underlain by the Ordovician unconformity, the Ellenburger Group, or the Viola Limestone/Simpson group, depending on the area. It is divided into the Upper and Lower Barnett Shale units by the Forestburg Limestone in areas, and is overlain by the Upper Barnett Limestone and the Marble Falls Limestone (Figure 1).

The Fort Worth Basin was formed during the late Paleozoic Ouachita orogeny, a tectonic event of thrust-fold deformation resulting from continental collision (Pollastro et al., 2007). Loucks and Ruppel (2007) state that the basin is interpreted to have formed in a deep water slope to basinal setting, where sedimentation occurred primarily through suspension settling and density currents. They also state that Barnett strata deposition took approximately 25 m.y. to accumulate an estimated average thickness of 1100 ft of uncompacted sediments, which were later compacted by at least 50%.

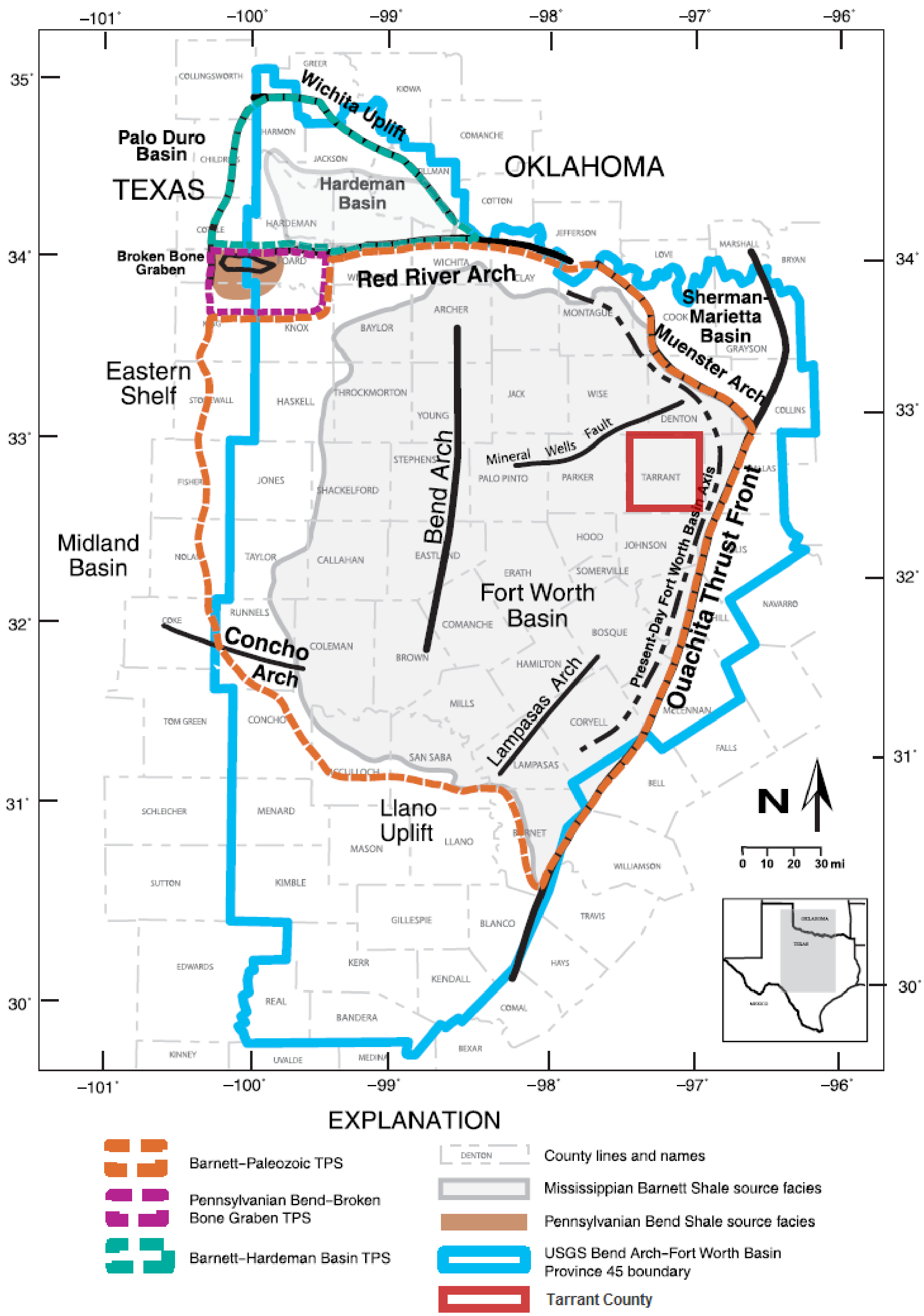

Figure 1. Map of the Bend-arch Fort Worth Basin depicting the major structures and the Tarrant County study area (modified from Pollastro et al., 2007).

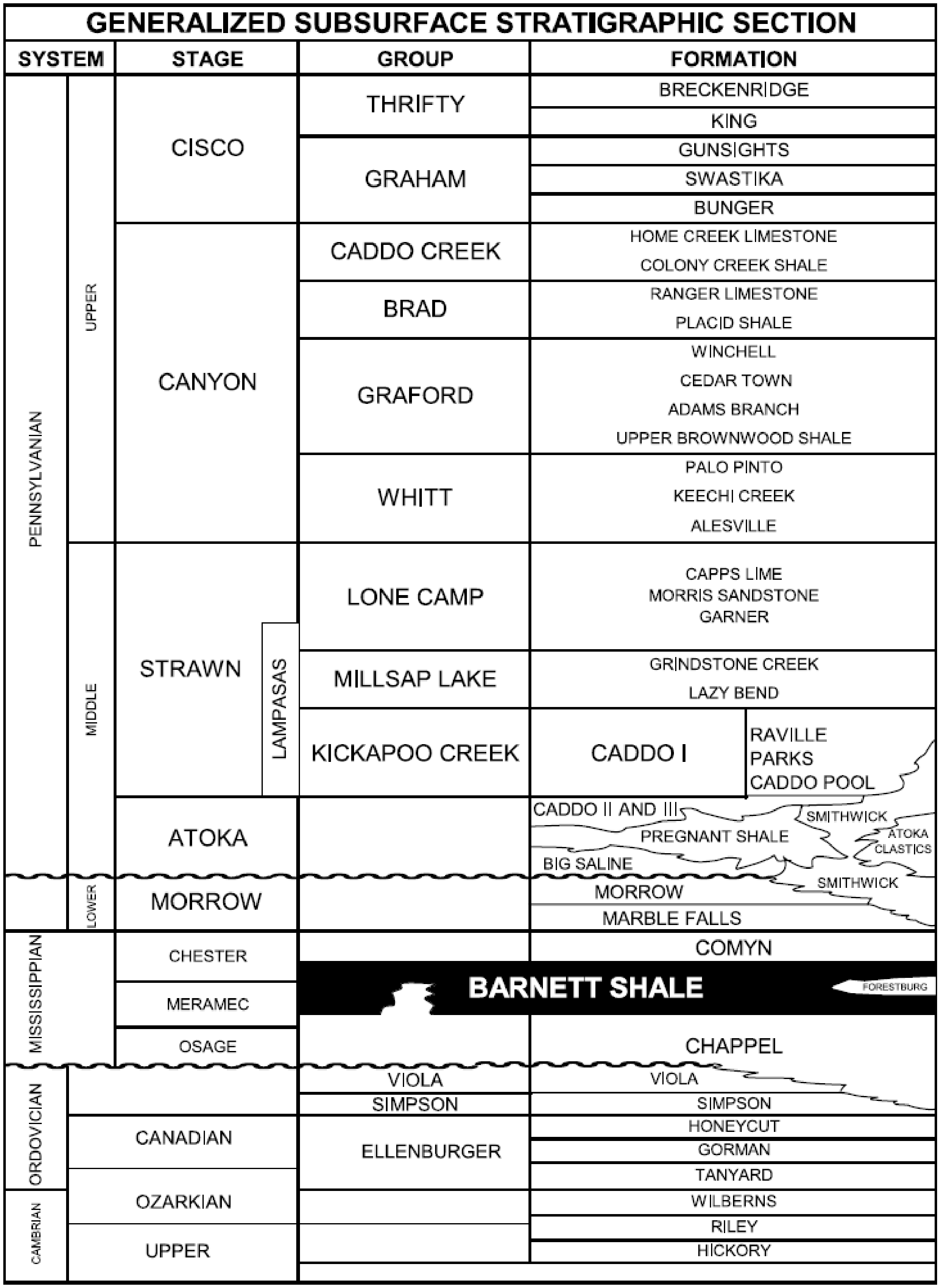

Figure 2. Generalized stratigraphic column on the Fort Worth Basin

(Modified from Jarvie et al., 2007).

2.2 Stratigraphy and Lithology

Different authors divide the Barnett Shale into a different number of lithofacies using different degrees of detail. Loucks and Ruppel (2007) state that the lower Barnett Shale contains more clay and less carbonate than the upper Barnett shale. They divide the Barnett Shale into three general lithofacies: (i) a laminated silicious mudstone; (ii) a laminated argillaceous lime mudstone or marl; and (iii) a skeletal, argillaceous lime packstone. Each facies contains pyrite and phosphate, and carbonate concretions are common within the Barnett Shale. Jarvie et al. (2007) divide the Barnett Shale into five lithologies: (i) a black shale; (ii) a lime grainstone; (iii) a calcareous black shale; (iv) a dolomitic black shale; and (v) a phosphatic black shale.

The most dominant mineral in the Barnett is biogenic silica. Other dominant components are clay to silt-sized calcite and dolomite and calcite-dominated skeletal debris. Generally the clay content in the Barnett Shale ranges from over 40% to less than 5% (Jarvie et al., 2007; Loucks and Ruppel, 2007). As a result it has been described as a siliceous mudstone or a fine-grained siltstone in northern portions of the Fort Worth Basin (Loucks and Ruppel, 2007).

The Barnett Shale's composition, low porosity, and permeability, require an integrated interdisciplinary study for a robust hydrocarbon production program. The following chapter discusses the theory behind the three methods used in this investigation: (a) monitoring of induced hydraulic fractures, (b) analysis of volumetric curvature seismic attributes, and (c) analysis of seismic acoustic impedance inversion.

3. THEORETICAL BACKGROUND

3.1 Hydraulic Stimulation and Microseismicity

The low values of matrix porosity and permeability of unconventional shale reservoirs like the Barnett Shale formation require techniques such as hydraulic fracturing to have economically viable production. Induced fracturing creates rough fracture surfaces and permeability by opening natural fractures and improving reserve recovery for a given well (Rutledge and Phillips, 2003; Gale et al., 2007; Miskimins, 2009). In general, induced fracture networks propagate perpendicularly or nearly perpendicularly to the minimum horizontal stress (S_{Hmin}), enhancing permeability and thereby drainage of the stimulated area. Based on the assumption that increased permeability and drainage area results in increased production, wells drilled perpendicularly to the maximum horizontal compressive stress direction (parallel to the minimum horizontal stress) should maximize stimulation (Daniels et al., 2007; Gale et al., 2007). Nevertheless, hydraulic fracturing is a time-dependant, path-of-least-resistance process. The stress regime may change during stimulation due to the presence of preceding fractures (Miskimins, 2009). By monitoring the dynamics of rock failure throughout the injection process using microseismic mapping, fracture propagation and drainage patterns may be characterized and the stimulation optimized.

Microseismic events associated with hydraulic fracturing present frequency content from 200 to 1000 Hz, and in some cases up to 2000 Hz (Warpinski, 2009). Such high frequencies require specialized monitoring techniques. Two main methods of monitoring microseismic activity currently dominate the oil industry: surface-based and downhole-based seismic monitoring. The surface-based method allows for large surface receiver array apertures and permits study of the complexities of fracture development over large areas, but suffers from surface noise and attenuation of higher frequencies (Lakings et al., 2006). Downhole-based microseismic images a smaller area, provides a cost-effective method with high vertical resolution, but suffers from low lateral resolution. Recent downhole monitoring techniques use several monitoring wells to address lateral resolution issues associated with single well monitoring.

Downhole microseismic mapping operations consist of one or more treatment wells (for injection) and at least one nearby monitoring well (typically less than 2000 ft.), with distance depending on the formation and its structural characteristics and attenuation. For monitoring it is necessary to construct a *P*- and *S*- velocity depth model of the subsurface. Geophone orientations are computed from the measured signal and the known locations of perforation shots. The difference between arrival times of *P*- and *S*-waves provides the distance of the events to the receivers. The particle motion (or polarization) provides event azimuth and elevation (Le Calvez et al, 2005). To obtain high signal strength the optimal positioning of the geophone array is straddling the zone of interest, since the differentiation of the P and S events based on moveout is more easily accomplished because of longer travel paths (Le Calvez et al., 2005; Eisner et al., 2009; Warpinski, 2009). It has been proposed that positioning receivers above the Barnett Shale formation could minimize the refracted energy and result in simpler waveforms, albeit with lower amplitudes (Warpinski, 2009).

Microseisms can be defined as small earthquakes along preexisting zones of weakness, generated by perturbations in stress and pore pressure associated with hydraulic fracturing (Rothert and Shapiro, 2003). Rothert and Shapiro (2003) hypothesize that a diffusive process of pore pressure relaxation reduces the effective normal stress. This activates motion along critical cracks, triggering microseismic activity. Rutledge and Phillips (2003) state that the dominant source mechanism is shear slip induced by elevated pore pressure, which reduces normal stress along preexisting fractures. They also consider that slip may occur near tips of fractures due to the large shear stresses generated by tensile opening. Their studies concluded that microseismic clouds represent shear stress released on surrounding fractures that are favorably oriented for slip.

Miskimins (2009) demonstrated that hydraulic fracture development does not usually occur as a simple bi-planar system, but in a complex system of multi-fracture strands that extend several hundred or thousands of feet in multiple directions. This creates a stimulated reservoir volume as opposed to the traditional single-plane fracture drainage profile.

Even though the Barnett Shale is relatively brittle due to its high silica composition, significant stimulation is necessary for production (Jarvie et al., 2007). Previous studies agree that seismicity associated with hydraulic fracturing is triggered along critically-stressed, preexisting fractures (Rothert and Shapiro, 2003), and studies of the shear activation of fractures indicate a strong correlation between induced seismicity and low-impedance flow paths. However, most originally open fractures in the Barnett Shale formation are now sealed with carbonate cement (Gale et al., 2007; Jarvie et al. 2007; Pollastro et al., 2007) and would intuitively seem stronger than the surrounding formation. New fractures would then preferentially occur in previously unfractured rock (Rutledge and Phillips, 2003). However, Gale et al. (2007) found that the calcite in the

Barnett Shale fractures does not grow in crystallographic continuity with the grains in the wall rock, i.e. no crystal bonds exists between the wall rock and the calcite cement, unlike quartz in cement in tight-gas sandstone fractures. As a result, the tensile strength of the contact between the calcite fracture fill and the shale wall rock is low in the Barnett Shale. In fact, Gale et al. (2007) state that the fracture-cement fills in the Barnett Shale are naturally parted from the wall rock, leading to weak fracture-host boundary bonding, and that the pre-existing fractures do provide a potential flow network towards the wellbore.

3.2 Curvature from 3D Seismic Data Volumes

Surface seismic measurements do not directly map fractures, but they can map larger scale faulting, folding, and flexures. In general, geoscientists infer the presence of fractures through the use of a tectonic deformation model, with fracture swarms being concentrated in more tightly folded and faulted zones. The type of fracture depends on the thickness and lithology of the rock layer and the direction of the three principal stresses at the time of deformation (Nelson, 2001).

Seismic attributes such as volumetric curvature computed from 3D surface seismic data allow us to make fracture predictions in the subsurface. Ideally, these fracture predictions are validated through image logs, production data, tracer data, or in this case through microseismic reactivation of paleo-zones of weakness.

We have established in the previous section that hydraulically-induced microseisms tend to occur within preexisting faults and fractures. The curvature attribute allows mapping of structural features such as folds and flexures in a surface seismic volume, which can represent existing faults and fractures. Applying the curvature attribute to the area of study can serve as a tool to predict where microseisms will occur and link surface seismic with microseismic.

Studies have shown favorable connections between curvature attribute and fractures (Massaferro et al., 2003; Lisle, 1994; Al-Dossary and Marfurt, 2006; Blumentritt et al., 2006). Massaferro et al. (2003) found vertical image log fractures to be consistent in direction and intensity with the fractures predicted through curvature analysis. Lisle (1994) found excellent correlation between Gaussian curvature and fracture density as measured on outcrops. Most positive or most negative curvature provides a more detailed and less ambiguous attribute for defining lineaments related to regional or local stresses than Gaussian curvature (Blumentritt et al., 2006).

Roberts (2001) defines curvature of a surface at a particular point as the "inverse of a circle's radius which is tangent to that surface at that point" (Figure 3). By fitting a quadratic surface to the surface seismic data and using the coefficients of the quadratic equation, curvature can be determined at every point on a gridded surface. "Since an infinite number of circles in normal planes of different azimuths may be tangent to the surface at any given point, the curvature of the tangent circle with the smallest radius is defined as the maximum curvature (k_{max})". This circle may lie below the plane and have a positive value of k_{max}, or above the plane and have a negative value of k_{max}. The minimum curvature (k_{min}) is defined as the curvature of the tangent circle perpendicular to the maximum curvature (k_{max}). For interpretation, it is often more useful to use the most principal positive curvature (k_1) and most principal negative curvature (k_2), where

$$k_1 = \mathrm{MAX}\ (k_{max}, k_{min}) \tag{1}$$

$$k_2 = \mathrm{MIN}\ (k_{max}, k_{min}) \tag{2}$$

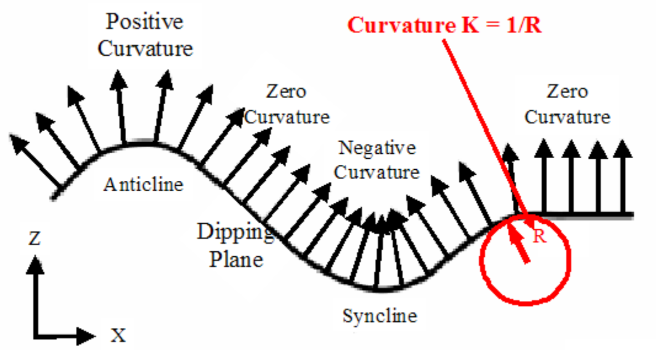

Figure 3. Two-dimensional curvature, where by convention, positive curvature is concave downward, and negative curvature is concave upward (from Roberts, 2001).

To relate the curvature attribute with the structural characteristics of the subsurface, 3D quadratic shapes can be described using values of k_1 and k_2. The six basic shapes are the bowl, dome, ridge, valley, saddle, and the plane. A bowl shape presents negative curvature values for k_1 and k_2 while a dome shape presents positive values for both, and a plane has zero values for both k_1 and k_2. The different shapes resulted from different k_1 and k_2 values are described in Figure 4.

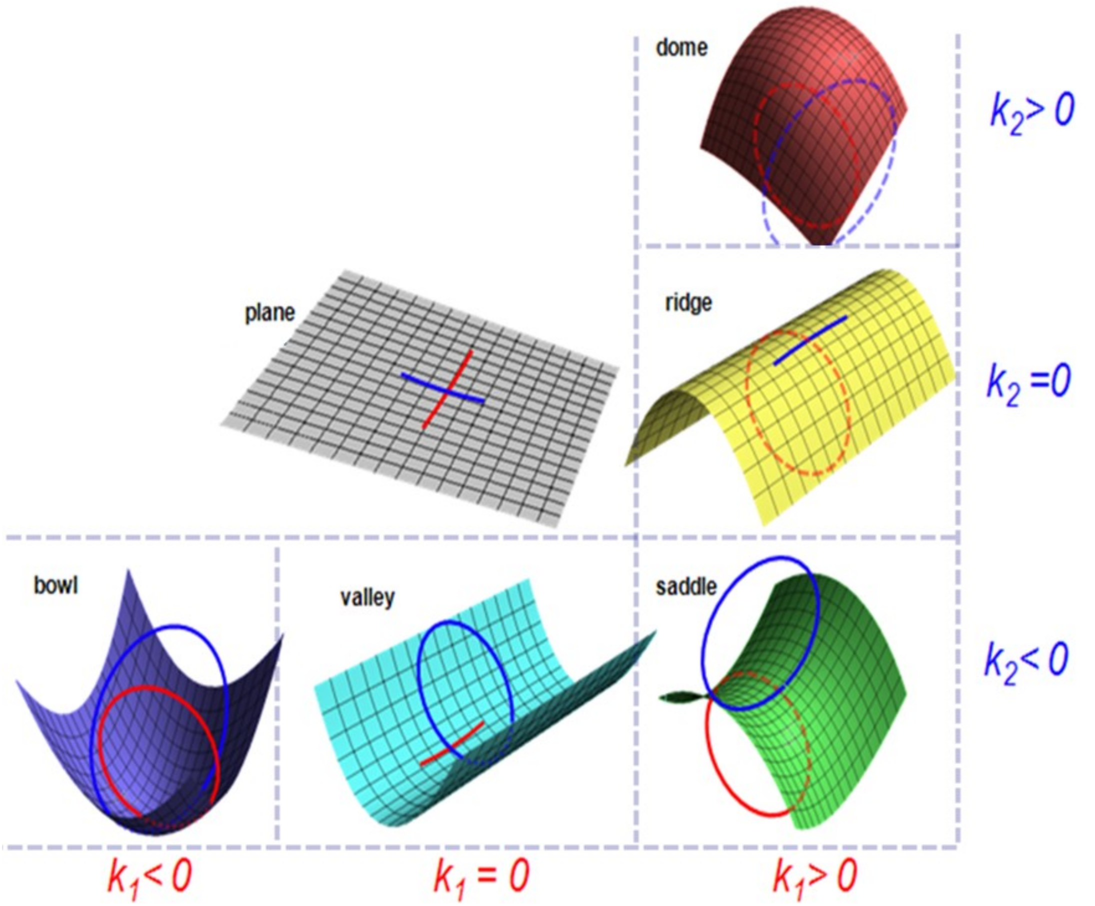

Figure 4. Three-dimensional quadratic shapes of most-positive and most-negative principal curvatures (k_1 and k_2) (modified from Mai, 2010).

For this investigation I use volumetric curvature rather than surface curvature, since the latter may introduce interpreter bias and picking errors. Al-Dossary and Marfurt (2006) describe volumetric curvature as a two-step process, in which the first step uses a moving-analysis sub-volume to estimate volumetric reflector dip and azimuth for the best-fit tangent plane for each sample within the seismic volume. Curvature is calculated in the second step from adjacent estimates of dip and azimuth.

Since geologic structures present curvature of different wavelengths, I analyzed both short and long curvature wavelength imaging. Short wavelength enhances details within intense, localized fracture systems, while long wavelength enhances subtle flexures correlative to fracture zones below seismic resolution, often difficult to observe in conventional seismic (Chopra and Marfurt, 2007). The fractional derivative approach for estimating volumetric curvature introduced by Al-Dossary and Marfurt (2006) is defined as

$$F_u(\partial u/\partial x)=-i(k_x)^{\alpha}F(u) \tag{3}$$

where F refers to the Fourier transform, u is an inline or crossline component of reflector dip, and α is a fractional real number ranging from 1 (resulting in the first derivative) and 0 (resulting in the Hilbert transform) of the dip (Al-Dossary and Marfurt, 2006). By decreasing the contribution of low or high frequencies, the bandwidth is shifted towards longer or shorter wavelengths respectively. For this study long and short wavelength were obtained with values of α=0.25 *and* α=0.85 respectively.

3.3 Seismic Inversion

My hypothesis in this thesis is that the material properties of density, acoustic impedance, and V_p/V_s ratio can be correlated to zones of hydraulically-induced microseismic fractures. After correcting for attenuation, seismic amplitudes measured at the Earth's surface are a function of changes in impedance. Using this fact, we can extend measured impedances from wells throughout seismic volumes after careful well-seismic calibration using a process called seismic inversion. The resulting impedance volume can be used as a characterization tool for reservoir exploration and development, and can even show how properties change as a consequence of ongoing production by the detection of gas fronts or induced fractures.

Seismic inversion is based on the convolution of the seismic wavelet and the Earth's reflectivity through a forward model:

$$S_t = (r_t * w_t + n_t) \cdot a_t , \qquad (4)$$

where S_t = the seismic trace,

r_t = the earth's reflectivity,

w_t = the seismic wavelet,

n_t = additive noise, and

a_t = amplitude scaling.

Reversing this process by reducing the noise, deconvolving the wavelet, and restoring the original amplitudes, we can obtain the Earth's normal incidence reflectivity values. Since our seismic data are band-limited and countermined by noise, this reversal is never completely achieved, providing an approximation to the true impedance model. The normal incidence reflectivity values relate to the acoustic impedance values through the following equations:

$$Z_{t+1} = Z_t \,[\, (1+r_t\,) \,/\, (1-r_t) \,] \qquad (3)$$

where $Z_t = \rho_t V_t$ = acoustic impedance of layer t,

ρ_t = density,

V_t = compressional wave velocity,

and layer t overlies layer $t + 1$.

Although simpler and more economical than pre-stack seismic inversion, post-stack seismic inversion has a noticeable disadvantage. The stacked traces are used as if they have normal incidence when in reality the summed traces contain amplitude vs. offset (AVO) effects. The resulting inverted volumes do not represent the true reflectivity of the subsurface. Pre-stack inversion takes into account the amplitude variations with offset and can not only overcome these limitations, but also provide additional information about the subsurface.

I used a commercial model-based pre-stack inversion algorithm that requires angle dependent wavelets and angle stacks and results in estimates of *P*-impedance (Z_p), *S*-impedance (Z_s) and density. This algorithm starts with an initial impedance model of the earth's geology which is updated using the conjugate gradient method until the derived synthetic seismic section best fits the observed seismic data (Hampson et al., 2005). To control the quality of the results, forward modeling of the resulting *P*- and *S*-impedance volumes and the use of AVO equations like Zoeppritz's equations should result in pre-stack synthetic seismic gathers that very closely match the recorded seismic stack (Goffey, 2009).

Three assumptions are made in the algorithm used for this study. These are that (i) the linearized approximation for reflectivity holds, (ii) reflectivity as a function of angle can be approximated by the Aki-Richards equations, and (iii) there is a linear relationship between *P*-impedance and both *S*-impedance and density.

Once the *P*- and *S*-impedance volumes have been generated they can be used to calculate the Lamé parameters of incompressibility, λ, and rigidity, μ. Incompressibility is more sensitive to the pore fluids than to the matrix, and for elastic materials rigidity is only influenced by the matrix connectivity (Dufour et al., 2002).

Since:

$$V_P^2 = (\lambda + 2\mu)/\rho \ , \tag{4}$$

$$V_S^2 = \mu/\rho \tag{5}$$

$$Z_P = \rho \ V_P, \text{ and} \tag{6}$$

$$Z_S = \rho\, V_S \tag{7}$$

The velocities can in turn be related to impedance in the following manner;

$$\lambda\rho = Z_P^2 - 2Z_S^2 \text{ , and} \tag{8}$$

$$\mu\rho = Z_S^2 \tag{9}$$

Goodway et al. (1997) also show that $\lambda\rho < \mu\rho$ for gas zones while $\lambda\rho > \mu\rho$ indicates thin, tight shale breaks. They state that when comparing Z_P vs. Z_S cross plots with $\lambda\rho$ vs. $\mu\rho$ (LMR) cross plots, the LMR plots better isolate lithologic properties and gas zones. Similarly, Aibaidula and McMechan (2009) state that for clastics, $\lambda\rho$ decreases with increasing gas content, porosity, and decreasing shale content.

The V_p/V_s ratio ($= Z_P/Z_S$) is often used in pore fluid and lithology identification because compressional waves are sensitive to fluid changes, where shear waves are not. Dvorkin et al. (1999) and Vanorio and Mavko (2006) have both stated that the V_P/V_S ratio decreases with decreasing differential pressure in gas-saturated rocks. Aibaidula and McMechan (2009) find ranges of V_p/V_S ratios of 1.59 to 1.76 for sandstones, 1.84 to 1.99 for limestones, and values of 1.7 to 3.0 for shale derived from land seismic measurements. Values for gas were reported as ~ 2.0 for low gas saturation and ~1.6 for high gas saturation in sandstone (Aibaidula and McMechan, 2009). These variations in inverted parameters serve as sensitive probes to lithology and gas content, and I will employ them in my study to broadly analyze the effectiveness of stimulations using the available production history. Nevertheless, the conclusions described by Goodway et al. (1997) and Aibaidula and McMechan (2009) must be used only as reference until further validation, since porosity and permeability values from their sample formations likely differ from the values of the Barnett Shale formation.

4. APPLICATION OF THEORY FOR SURFACE SEISMIC ANALYSIS

The pre-stack and post-stack seismic volumes used in this investigation cover 14.2 square miles in Tarrant County, TX. Four vibroseis sources used 10 sweeps of 8 seconds each with a range of 10-110 Hz. The source interval was 311 ft and the receiver interval was 220 ft. The recording was carried out with a 2 ms sample rate and a CDP bin size of 110 by 110 ft.

4.1 Curvature Attribute

Volumetric curvature attributes have successfully highlighted features from folds and flexures to collapse features and carbonate buildups. By using long wavelength curvature as well as short wavelength curvature we can highlight broad and detailed aspects of our study region's geology. As discussed in Chopra and Marfurt (2007), "short wavelength curvature delineates details within intense, highly localized fracture systems. Conversely, long wavelength curvature often enhances subtle flexures correlative to fracture zones below seismic resolution and collapse features that result in broader depressions".

In this case long wavelength most positive and most negative principal curvatures show lineaments that trend parallel to the Mineral Wells and Ouachita Thrust Faults, as well as the Muenster Arch (Figures 5a and 5b). Short wavelength curvature also displays these regional features, as well as smaller features (Figures 5c and 5d) at azimuths parallel to the present day dominant northeast-southwest maximum horizontal stress trend and secondary perpendicular lineaments from secondary stress changes (Gale et al., 2007). The short-wavelength volumetric curvature also exhibits strong acquisition footprint which needs to be taken into consideration when interpreting stress patterns and existing fracture zones.

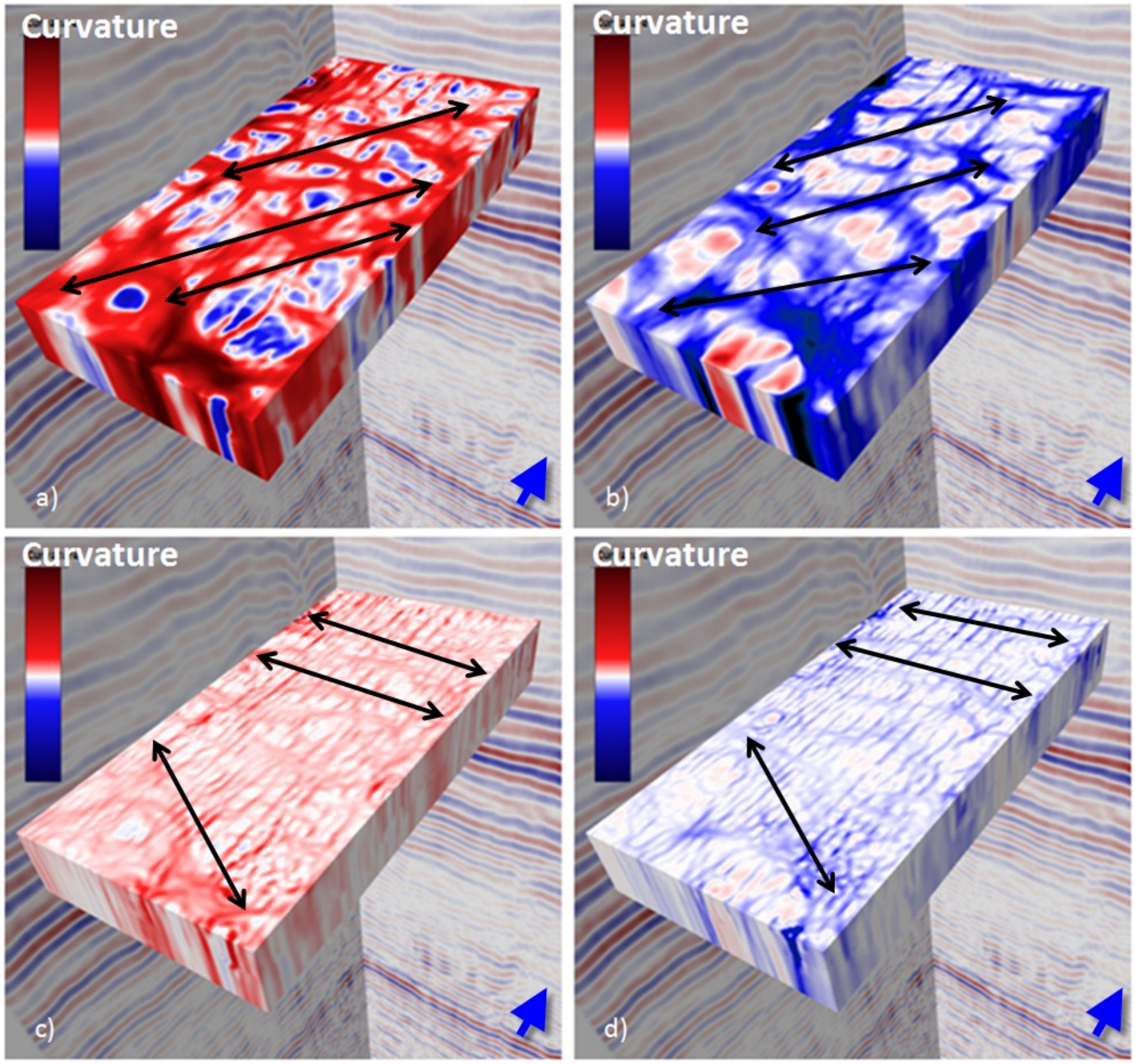

Figure 5. Strat-cubes with arrows showing predominant lineaments through a) long-wavelength most-positive curvature, b) long-wavelength most-negative curvature, c) short-wavelength most-positive curvature, and d) short-wavelength most-negative curvature. Note the strong acquisition footprint on the short-wavelength curvature volumes.

The curvature characteristics of the Marble Falls Limestone, Upper Barnett Shale, and Upper and Lower Barnett Shale are very similar to each other, with subtle differences. The limestone formations suffer more from acquisition footprint than the shale formations. In particular, the Marble Falls formation shows the N-S footprint most clearly**.** The curvature lineaments in both k_1 and k_2 form dense clusters in the shale formations compared to the limestone formations. This difference could be attributed to more intense deformation within the shales perhaps associated with their mineralogical composition. No noticeable differences in character were observed when comparing areas hydraulically fractured before or after the surface seismic acquisition.

4.2 Seismic Inversion

The goal of the inversion is to estimate the elastic rock properties in the subsurface, and coupled with microseismic events predict which shale facies are conducive to fracturing under hydraulic stimulation for hydrocarbon production.

Due to the less than 3° dip of the Barnett Shale, I used a pre-stack un-migrated volume without further processing. At the time of this study 274 wells had been drilled within the seismic survey. Only four of those wells had high-quality density, *P*- and *S*-wave velocity logs. These four wells were located in the northern, central, and southern portions of the seismic volume, providing a sufficient distribution of the measured properties in the area (Figure 6). It must be noted that it is common practice to log wells before any hydraulic fracturing operation. Assuming this is the case for the current investigation, the impedance model generated should theoretically represent the properties of the unfractured medium from which the logs originated.

A low frequency background model was constructed from seismic horizons and well logs filtered using a high-cut frequency of 10 Hz with a taper to 15Hz (Figure 7).

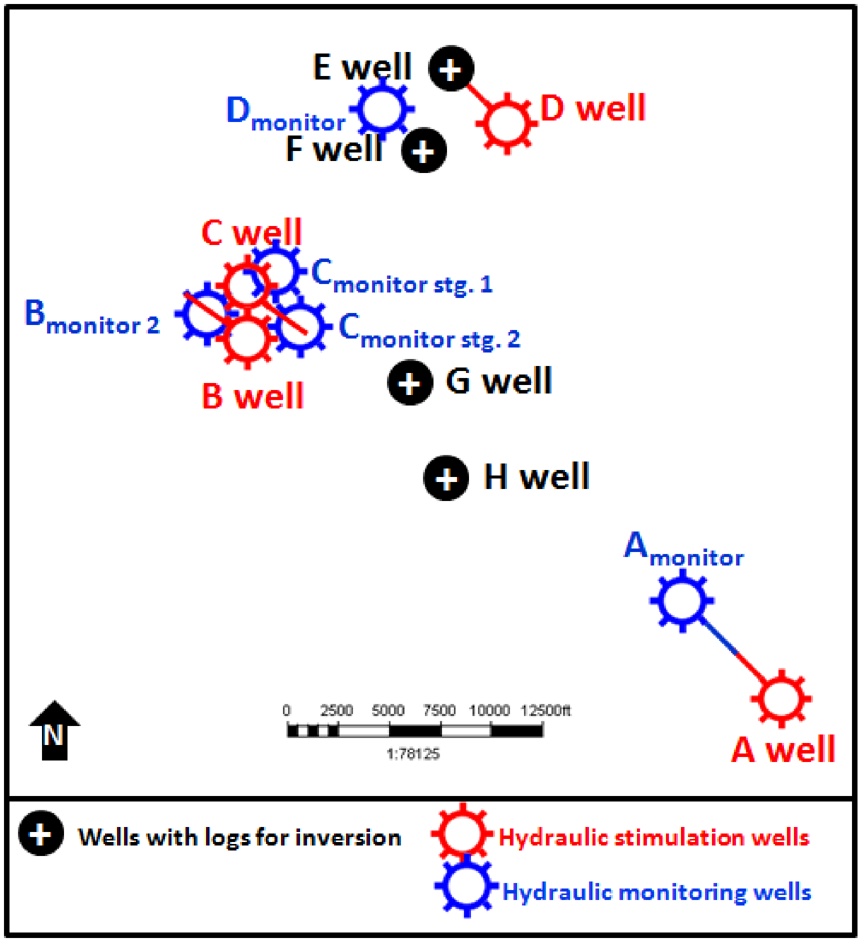

Figure 6. Location of wells with logs, hydraulic stimulation wells, and hydraulic monitoring wells.

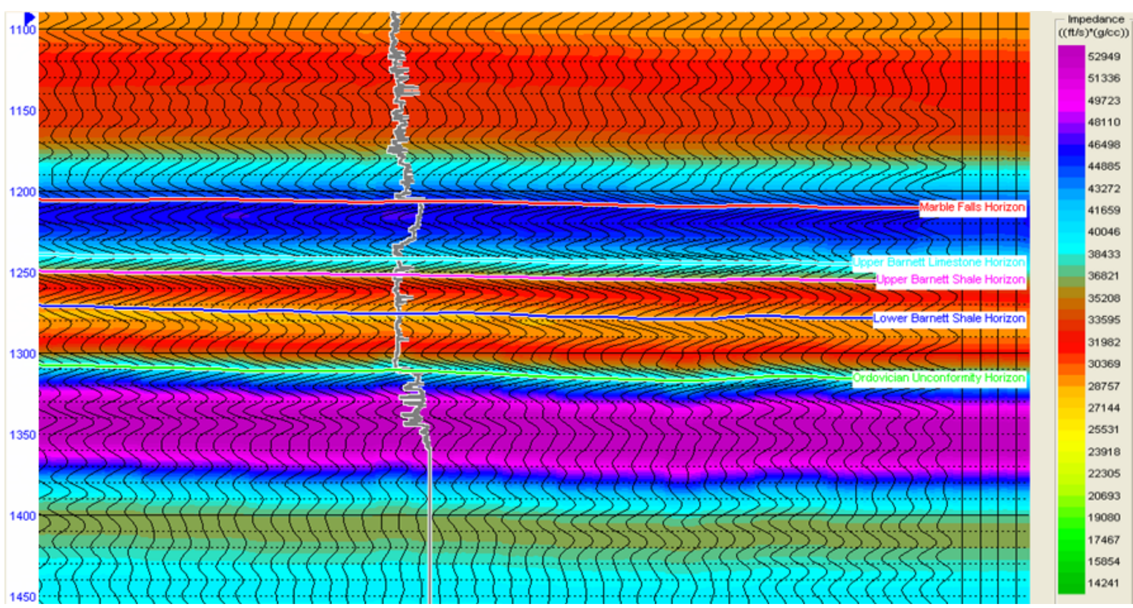

Figure 7. Initial Z_p model inversion. Formation tops and V_p log of well B are included for reference.

Near- (0°-15°) and mid-offset (15°-30°) zero phase wavelets, were extracted from the seismic volume (Figure 8), decreasing the impact of possible AVO anomalies on the far offset associated with the un-migrated nature of the data. The wavelets were extracted from the interval between the top of the Marble Falls limestone formation and the bottom of the Lower Barnett Shale, from 1.1 to 1.4 seconds.

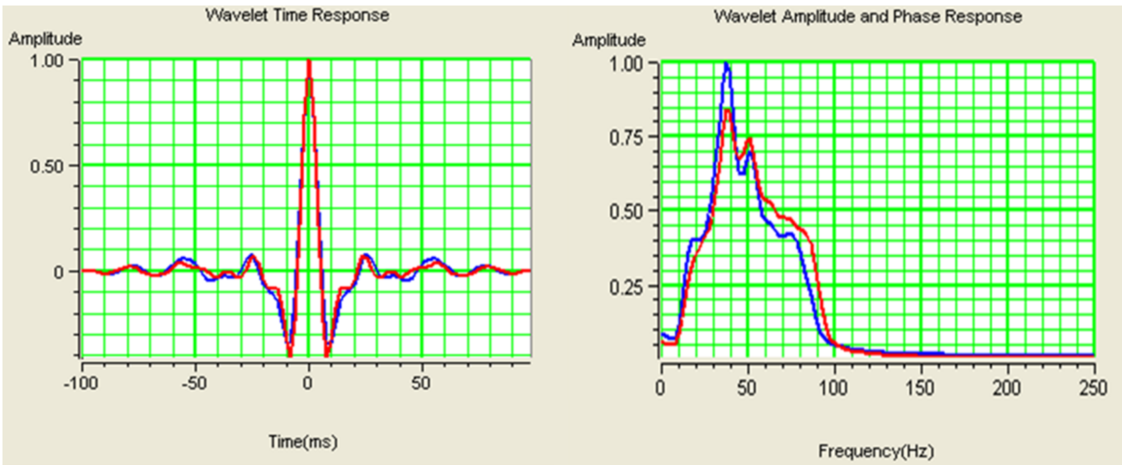

Figure 8. Near- and mid-offset wavelets extracted from pre-stack seismic gathers from 0°-15° (in red) and 15°-30° (in blue) between the top of the Marble Falls limestone and the bottom of the Lower Barnett Shale formation. Note the slight loss of high frequencies on the mid-offset wavelet due to NMO stretch.

The wavelets were used, along with a reflectivity model, to generate synthetics to mimic the recorded seismic traces between the areas of the Marble Falls formation and the Ordovician Unconformity. A correlation of R= 0.78-0.94 was achieved between the recorded seismic gathers and the inverted gathers along the target area, which I consider high for un-migrated data.

The average values of the inverted ρ, Z_p, Z_s, V_p/V_s ratio, $\lambda\rho$ and $\mu\rho$ within each formation are listed in Table 1. To account for possible interpretation bias, surfaces were also interpreted through the middle of the formations and values of each property were also extracted and averaged over a range of 5 ms on either side of the surface. The results were consistent with the values picked on the surface. The highest values of the inverted ρ, Z_p, Z_s, V_pV_s ratio, $\lambda\rho$ and $\mu\rho$ corresponded to the Marble Falls and the Upper Barnett Limestone. The results are consistent with studies from Aibaidula and McMechan (2009), where the shale formations have consistently lower density, impedance and V_p/V_s ratios than the limestone formations. Note that the inverted properties in the Upper and Lower Barnett Shale formations fall within the same range, indicating similar composition in comparison to the Marble Falls Limestone and Upper Barnett Limestone. Inverted $\lambda\rho$ and $\mu\rho$ values show similar behavior to the impedance values, as can be expected from their algebraic relationship to impedance (equations 10 and 11). The inverted Lamé parameters agree with Goodway et al. (1997), where $\lambda\rho < \mu\rho$ for gas zones, confirming the hydrocarbon potential of the Upper and Lower Barnett Shale.

	ρ (g/cm^3)			Zp (ft/s)*(g/cm^3)			Zs (ft/s)*(g/cm^3)			Vp/Vs unitless			λρ GPa*(g/cm^3)			μρ GPa*(g/cm^3)		
	Avg	Min	Max	Avg	Min	Max	Avg	Min	Max	Avg	Min	Max	Avg	Min	Max	Avg	Min	Max
M. Falls Ls.	2.64	2.60	2.68	40000	33000	46000	21500	19000	24000	1.88	1.68	2.04	62	30	100	42	30	55
U. Barnett Ls.	2.58	2.48	2.70	34000	27500	45500	20100	17500	23400	1.72	1.53	1.98	35	13	78	38	28	51
U. Barnett Sh.	2.52	2.43	2.61	32000	25000	37500	18800	16000	22000	1.66	1.46	1.80	24	4	46	34	24	48
L. Barnett Sh.	2.52	2.42	2.59	33000	25000	38000	19700	16200	22000	1.67	1.47	1.82	26	5	42	36	24	45

Table 1. Average values of inverted properties: density, *P*- and *S*-impedance, V_p/V_s ratio, and LMR. Values were extracted from surfaces in the middle of each formation and averaged within a range of the surfaces.

Based on studies from Aibaidula and McMechan (2009) that show that gas-saturated shales exhibit low $\lambda\rho$ and $\mu\rho$ values, I interpret the lower values on the $\lambda\rho$-$\mu\rho$ plots (Figure 9) as representing gas-saturated zones. High production from wells *B*, *D*, and *C* hint at the possibility that low $\lambda\rho$ and $\mu\rho$ values in the completed zones correspond to gas-saturated rock. Further, low production from wells *A* and *E* is associated with higher $\lambda\rho$ and $\mu\rho$ zones. Since compressional waves are more sensitive to fluid saturation than shear velocities, *Vp/Vs* ratio values can also be associated with production and gas-saturated zones in a similar manner as the Lamé parameters. The Upper and Lower Barnett Shale formations show lower values of V_P/V_S ratio associated with the unit's hydrocarbon potential, and wells *B* and *D* in this interval have higher production histories than wells *A* and *C*.

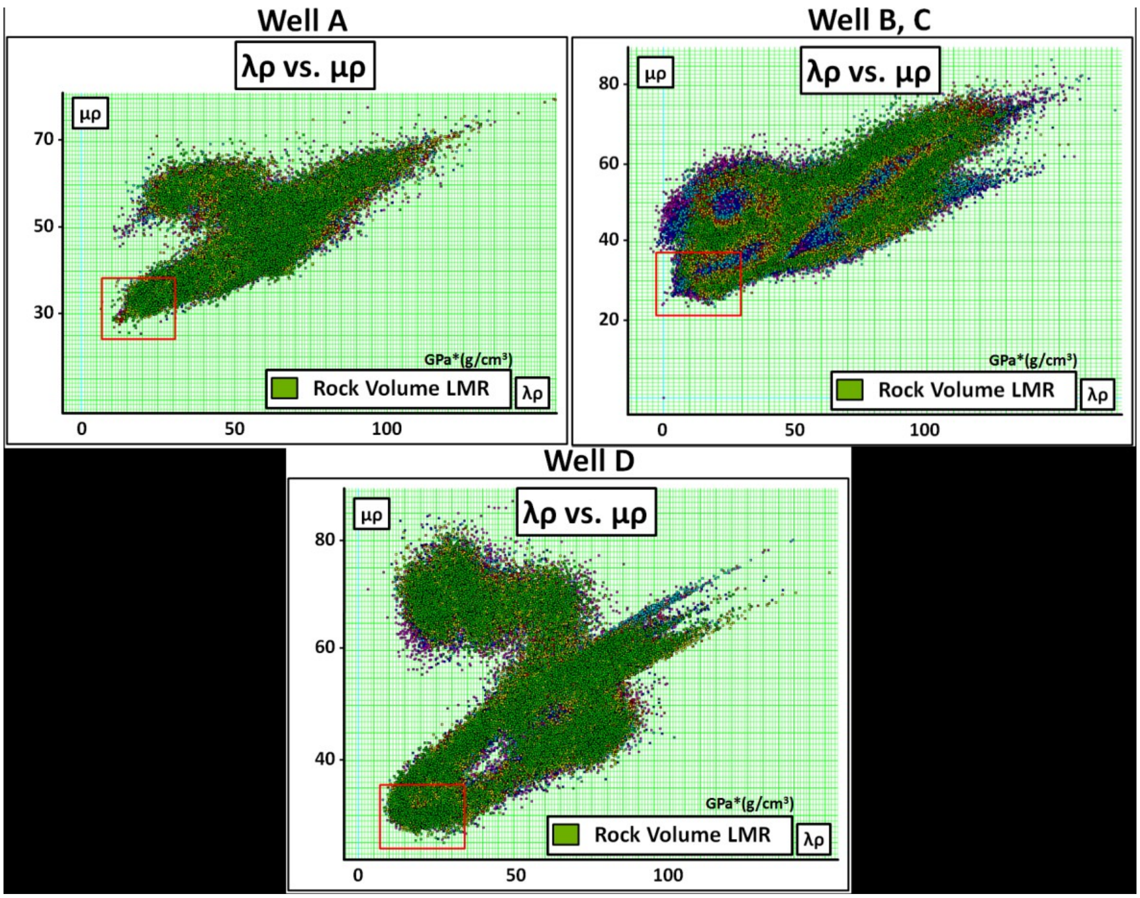

Figure 9. $\lambda\rho$ vs. $\mu\rho$ plots from values extracted from small volumes surrounding the stimulated wells. Following the conclusions of Aibaidula and McMechan (2009), the red squares represent the gas-saturated zones.

I extracted values of V_p/V_s ratio, $\lambda\rho$, and $\mu\rho$ from the inverted seismic volumes near the wellbores (Figure 10). V_p/V_s and LMR are low in the Barnett Shale with respect to other formations, but still show considerable variation. Lateral variation is observed in time slices at the horizontal portion of the stimulation wells.

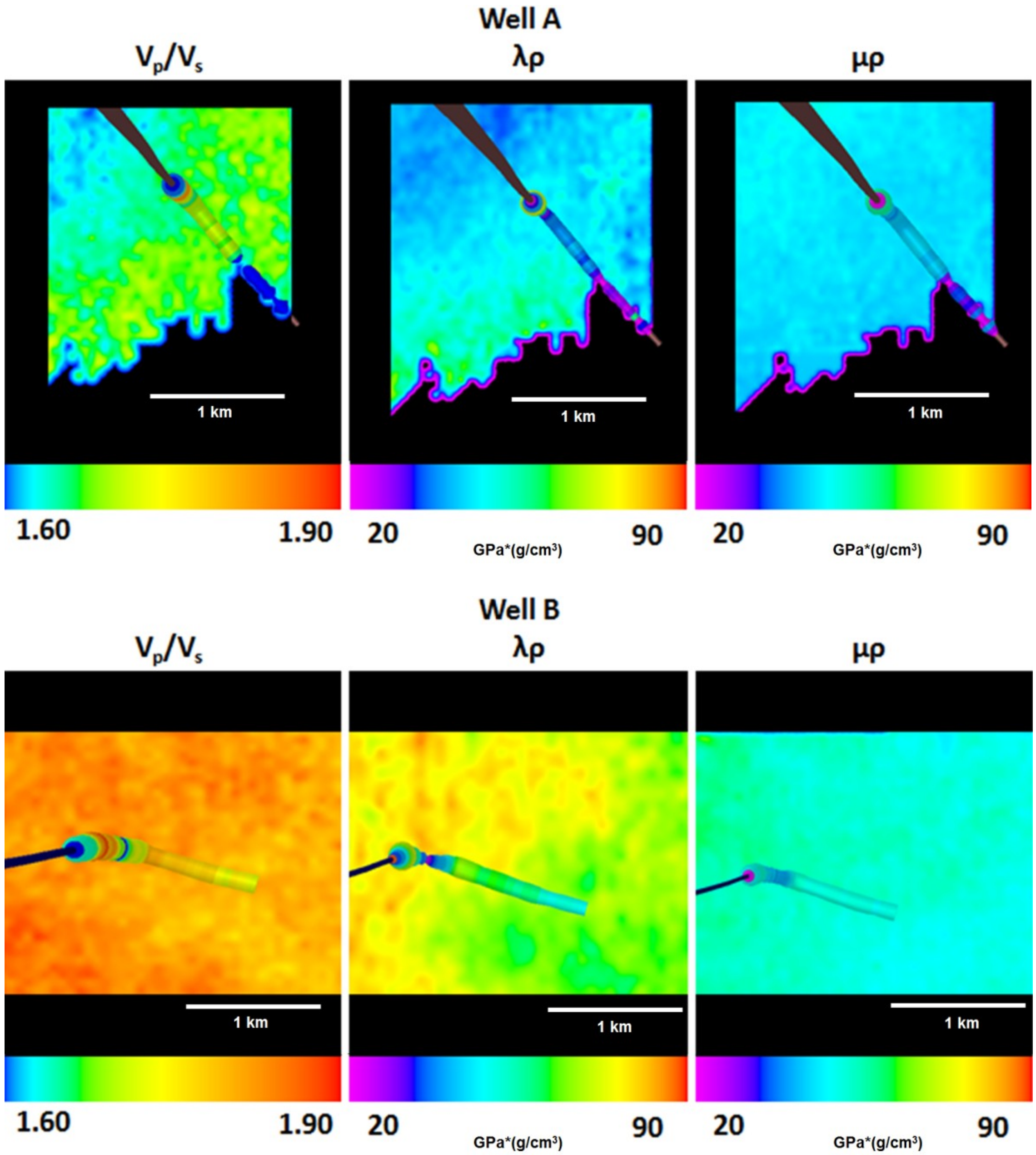

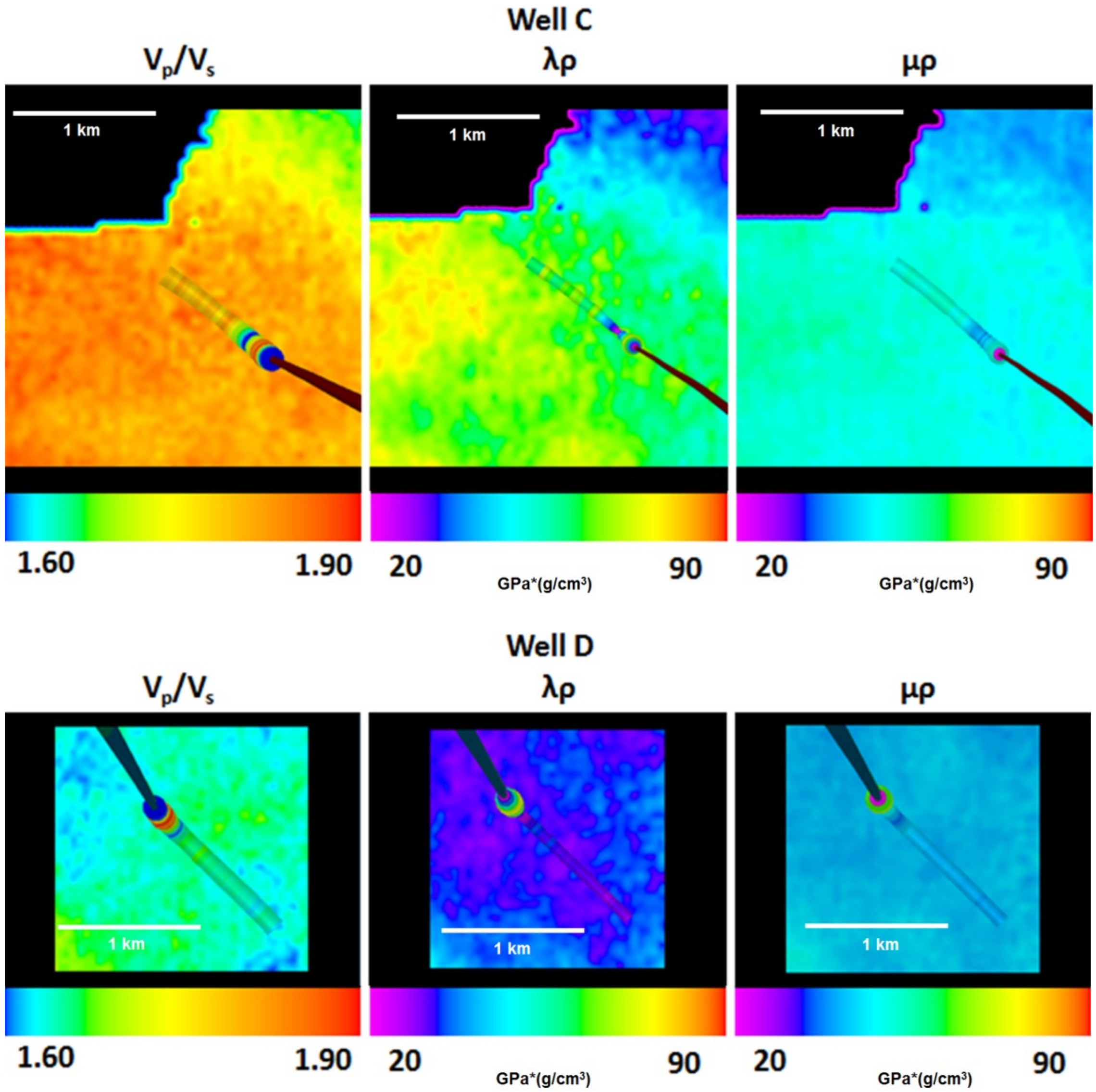

Figure 10. Time slices through the Lower Barnett at the level of wells A-D through Vp/Vs ratio and LMR volumes, with pseudlo-logs extracted from the corresponding volumes along the length of the wellbores. Note erroneous values on end of well A extracted from the edge of seismic volume.

5. MICROSEISMIC ANALYSIS

In order to measure microseismic events induced by the hydraulic fracture stimulation process monitoring wells were equipped with 12 down-hole three-component broadband (3-1500 Hz) geophones. These geophones were placed at 36.9 ft (~12 m) intervals starting at 150 ft (46 m) above the Marble Falls Limestone top to several feet above the Upper Barnett Limestone. The microseism dataset used here consisted only of processed event locations; processing parameters and location error bars are unknown. Stimulation wells *B*, *C*, and *D* were hydraulically fractured before the surface seismic acquisition, while stimulation well *A* was fractured after the seismic acquisition, which allows a comparative analysis of pre- and post-stimulation properties.

5.1 Microseism Interpretation

Mapped microseisms are a measure of the basin's local and regional stress history (Figure 11). Events preferentially align parallel to the current maximum horizontal stress direction (NE-SW), forming primary NE-SW stress lineaments and secondary perpendicular NW-SE lineaments. Tectonic deformation throughout the basin's history gave rise to the observed primary and secondary fracture lineaments that parallel the Ouachita Thrust Front, the Mineral Wells Fault, and the Muenster Arch (Gale et al., 2007; Loucks and Ruppel, 2007; Pollastro et al., 2007). Most seismicity associated with hydraulic fracturing is triggered along critically stressed, pre-existing fractures as expected, e.g. (Rothert and Shapiro, 2003).

Microseismic events appear to propagate parallel to the bedding (Figure 12) and are most intense on transition points between formations, suggesting that weakness planes between sudden lithology changes are susceptible to hydraulic fracturing and are potential drainage pathways. Wells B and C show dense microseism clouds in the lower Barnett Shale that generally lose intensity at the Ordovician Unconformity Viola

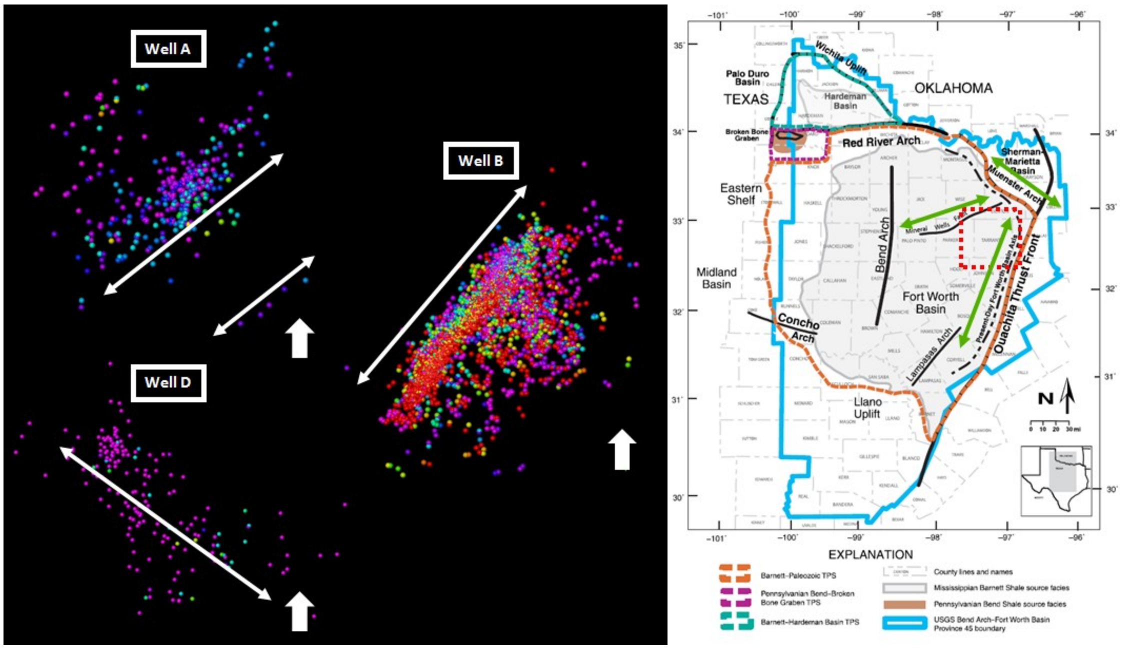

Figure 11. Mapped microseisms of wells A, B, and D (left) and regional map of the FWB's structures (modified from Pollastro et al., 2007) (right) show that the orientation of fracture lineaments formed by the microseismic clouds align parallel to the Ouachita Thrust Front, the Mineral Wells Fault, and the Muenster Arch.

surface (Figure 13) while propagating along the contact surface. Similarly, Lower Barnett Shale event clouds noticeably decrease in density at the high-calcite base of the Forestburg Limestone with the fracture system extending along the boundary laterally. A dense event cloud from the Upper Barnett Limestone also appears to stop or dissipate before reaching the denser Marble Falls Limestone. Microseism locations show that planes of formation contacts can act as fracture barriers, allowing only a few fractures to propagate through them. The Marble Falls limestone above the Barnett Shale has a higher fracture threshold than the shale (Jarvie et al., 2007), providing a barrier to stimulation. Although the high density of microseisms and extent of the induced fracture system within the Lower Barnett Shale is directly related to targeted stimulation, it can also be associated with the higher fracture threshold of the Upper Barnett Shale. I theorize that high silica and carbonate content of the Upper Barnett increases the density of the formation, hindering rock failure with a higher fracture threshold than the Lower Barnett Shale. Similarly, the less dense Lower Barnett Shale can fail with less stress than the Upper Barrnet because of its higher clay content (Jarvie et al., 2007; Loucks and Ruppel, 2007).

Energy information from the microseisms was available for wells *A* and *D*. Events for these two wells had an energy range of -4 to 1 Joules for well *A* and from -2.5 to 1 Joule for well *D*. Plots of recording time (sec) vs. energy released (Figure 13) show vertical lineaments that can be attributed to pressure buildup from the hydraulic pumping and subsequent fracture propagation periods. The data available were not sufficient to reach sustainable evidence of a lithology-energy relationship.

Given that the analyzed dataset was processed before this study and the raw data were not available, no location error data were available. Nevertheless, it is important to discuss the causes, impact, and quantification methods of microseismic location error. Acquisition geometry, picking error in varying noise environments, and velocity model error are the primary sources of uncertainty in microseismic event location (Eisner et al., 2009). Microseismic data sets recorded with downhole tools exhibit a distance-dependent error (location dispersion error), which causes a systematic spreading of events as the distance between source and receiver increases (Eisner et al., 2009; Warpinski, 2009; and Kidney et al., 2010). This is caused by the increase of uncertainty

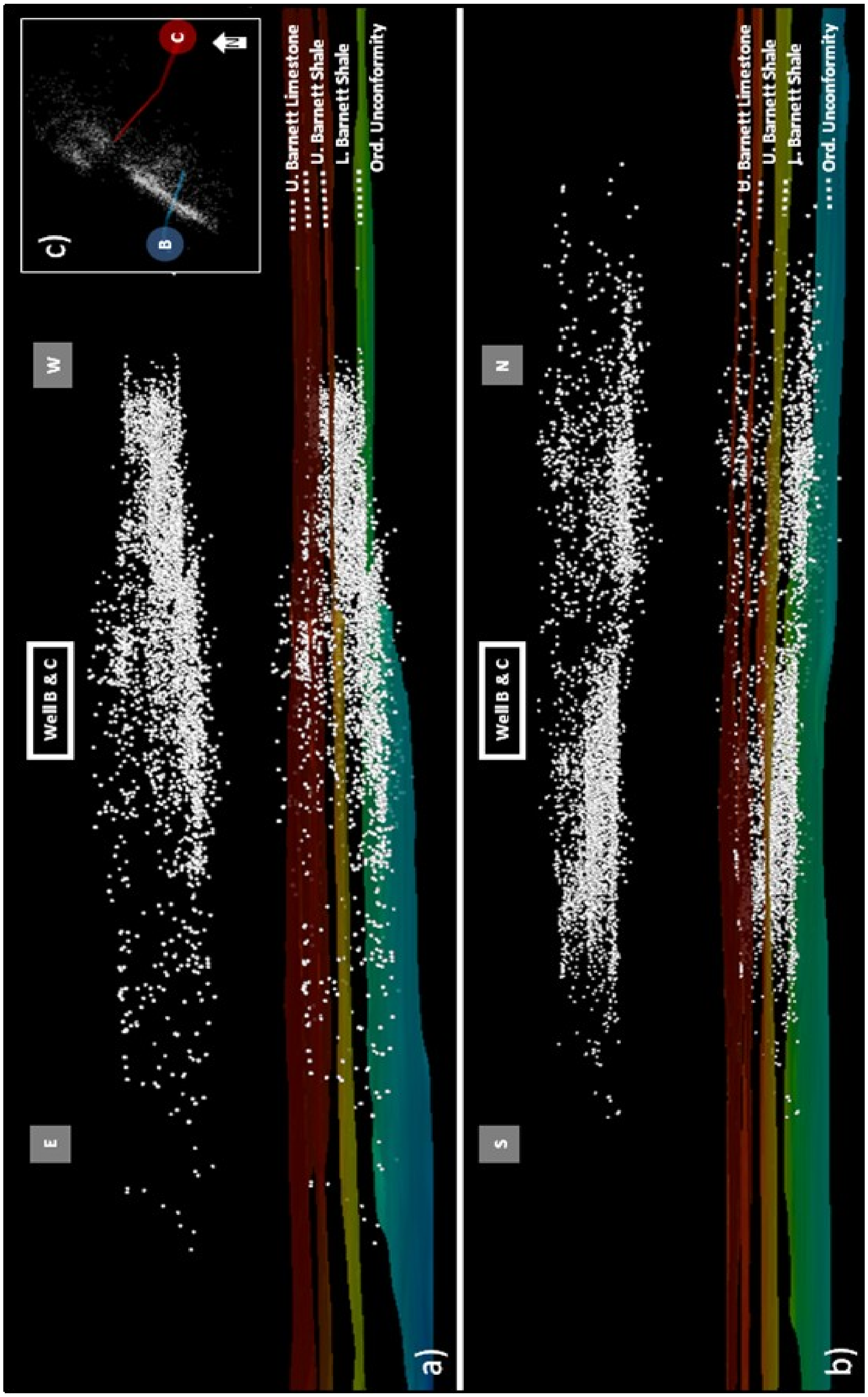

Figure 12. Side views from (a) north and (b) east of mapped microseisms from wells *B* and *C* with and without formation top surfaces. These views show horizontal lineaments that match transitions between formations, which act as vertical fracture barriers and possibly lateral weakness planes in some cases. (c) View from above.

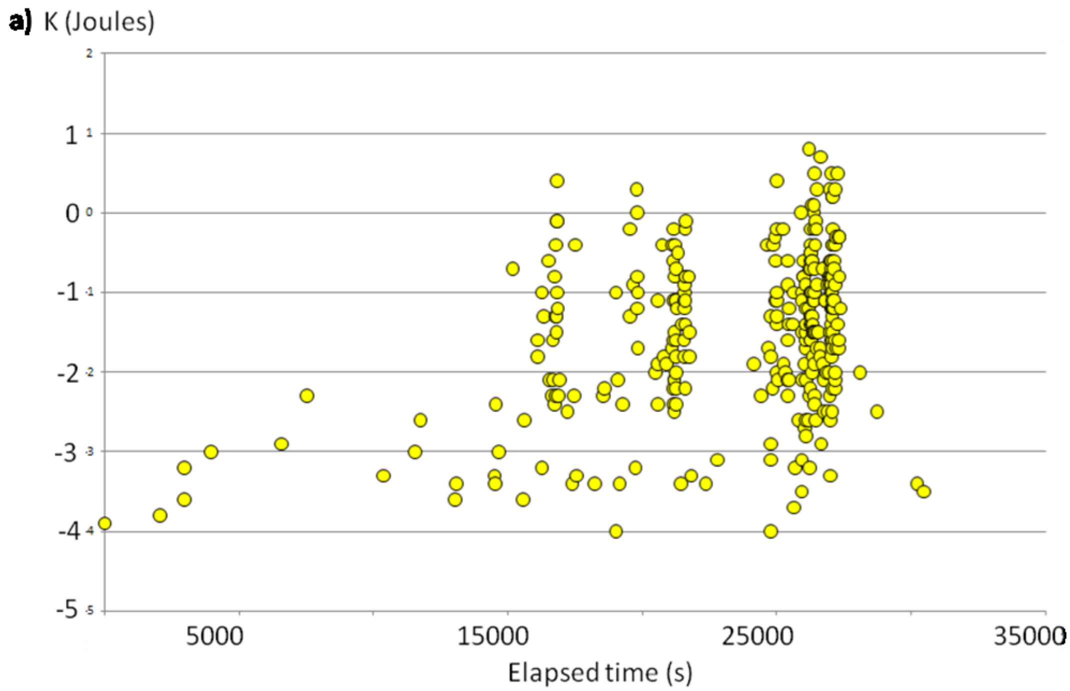

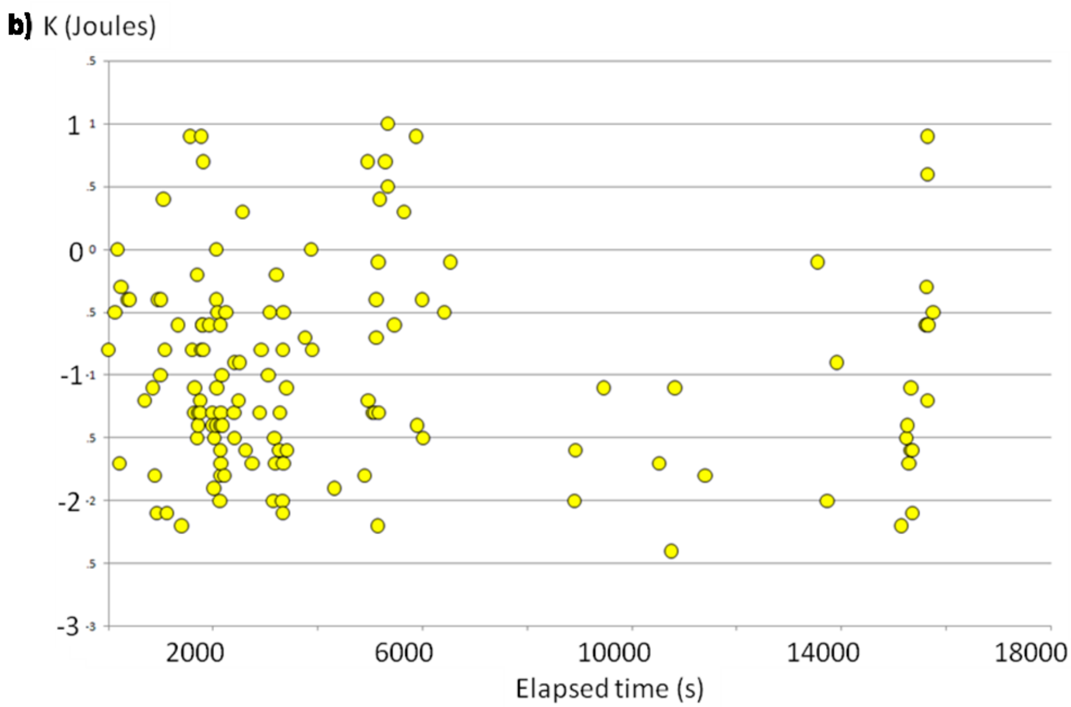

Figure 13. Plots of elapsed recording time and energy released during hydraulic stimulation of (a) well *A* and (b) well *D*. Plots show sudden bursts of fracture generation at different intervals, suggesting pressure buildup and subsequent release during rock failure.

in the velocity model and in the *P*- and *S*-wave hodograms in vertical monitor wells. Moving away from the source decreases recorded amplitudes by 1/distance through geometric spreading and lowers the signal/noise ratio (Warpinski, 2009). Further, vertical dispersion error increases with shorter sensor arrays and when sensors are available only above true event locations. Similarly, arrays with few sensors cause increased azimuth variation and therefore, lateral dispersion error. Angular uncertainty of a vertical monitoring well decreases as $1/\sqrt{n}$, where n equal the number of tools. The dispersion error can be quantified using Monte Carlo simulations or traveltime residuals, which provide a measure for the fit between the theoretical data and picked arrival times (Warpinski, 2009; Kidney et al., 2010). Eisner et al. (2009) and Kidney et al (2010) find that a borehole single vertical array can display from 1 to 10s of meters of vertical uncertainty, along with 10s of meters of horizontal uncertainty. Reprocessing of the dataset used in this study would yield the information needed for calculating high error zones and subsequent filtering, however the raw data were not available.

5.2 Microseisms and Volumetric Curvature

I computed the volumetric curvature attribute from a post-stack time-migrated seismic survey that covered all microseism areas except for stage 1 of well *C*, which was therefore omitted from my analysis.

The volumetric curvature attribute also correlate to the microseisms. In the most negative curvature volume, events occur away from the most negative values (Figure 14), favoring areas with high positive curvature in the most positive curvature volume (Figure 15), as hinted by studies of Mai et al. (2009).

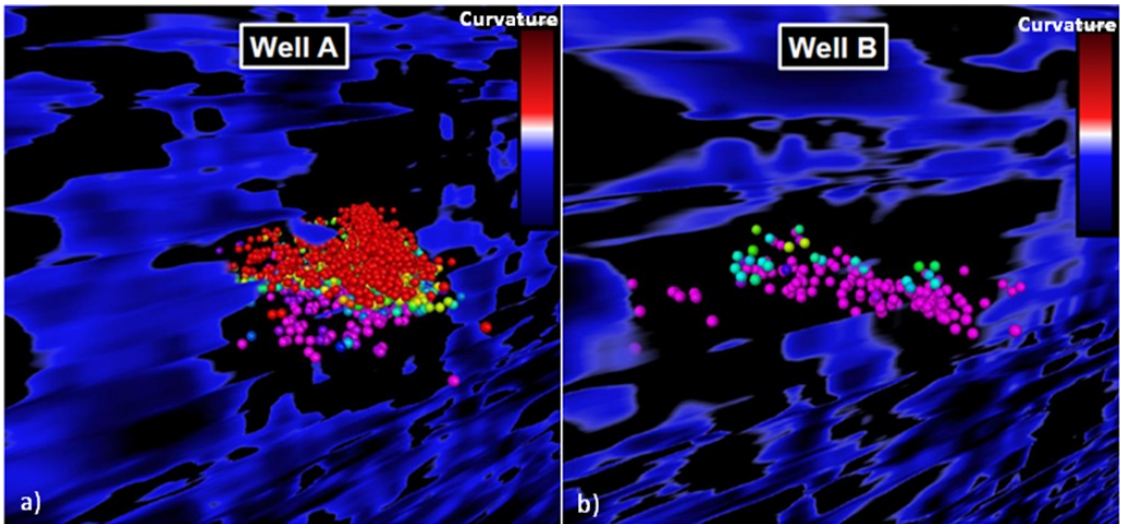

Figure 14. Long wavelength most negative curvature vertical cross sections through microseismic event clouds in a) well *A* and b) well *B*.

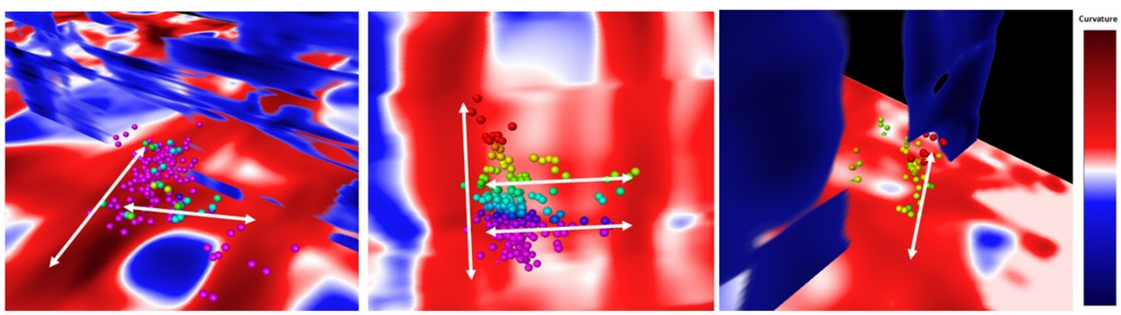

Figure 15. Long wavelength most negative curvature vertical cross sections with most positive curvature time slices through microseismic event clouds in a) well *A*, b) well *B*, and well *C*.

Figures 16 and 17 show the curvature values corresponding to the microseism locations along with the curvature values of the volume surrounding the hydraulic stimulation as a whole for both long and short wavelength curvature. Microseism locations correspond to positive short wavelength k_1 values for wells *A* and *D*, and negative values for wells *B* and *C* (Figure 16). Further, the mapped microseisms also show a strong correlation with predominately negative short wavelength k_2 values for wells *A* and *D*, *B,* and *C*. The long wavelength volumetric curvature relationship shows similar results (Figures

18 and 19). Microseisms in wells *A* and *D* located in negative long wavelength k_1 values and positive long wavelength k_2 values. Wells *B* and *C* presented a high incidence of events in positive long wavelength k_1 values and slightly negative long wavelength k_2 values.

Values of long wavelength curvature for the volume surrounding the hydraulic stimulation vary when compared to the bell-shape character of short wavelength values. For verification purposes, similar relationships were established with long wavelength values of the complete seismic survey (Figures 20 and 21). This shows the range of k_1 and k_2 values throughout the extent of the survey, indicating simpler single-mode histograms that can be simply related to the microseism curvature values.

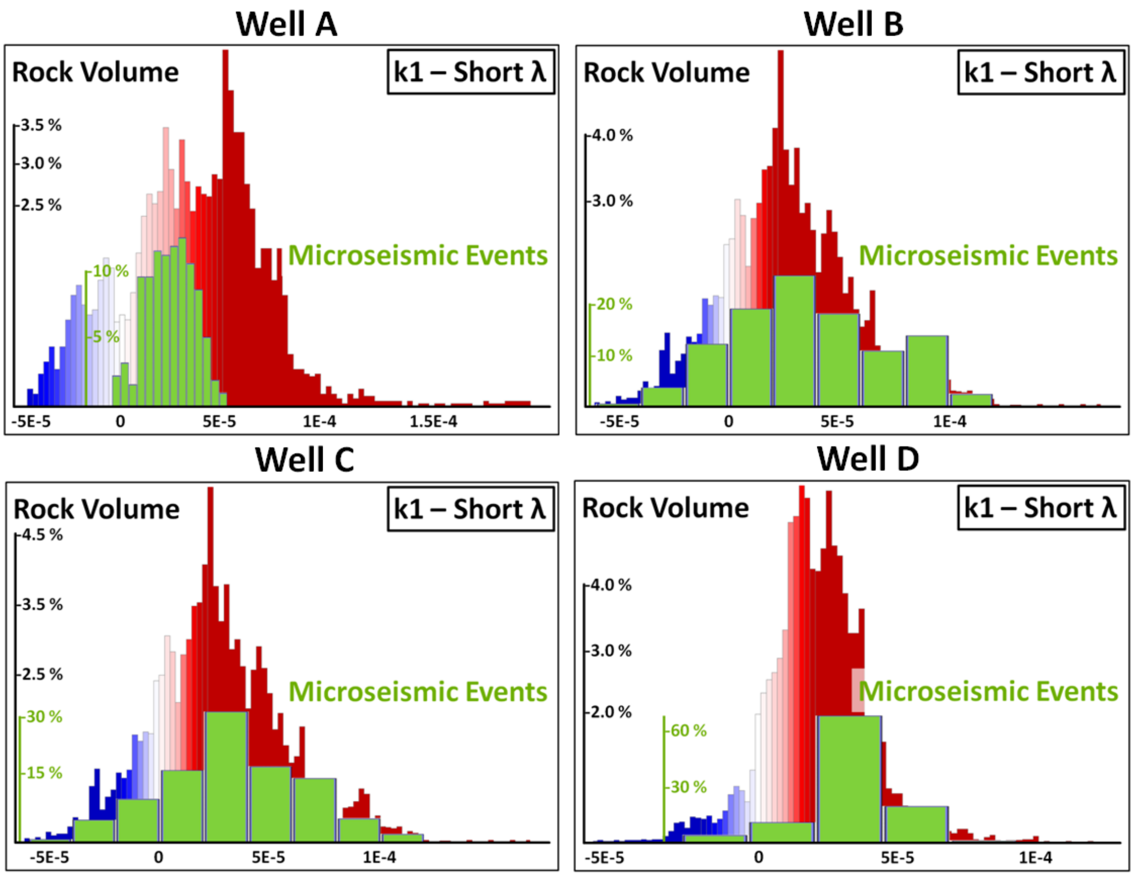

Figure 16. Short wavelength k_1 values of recorded microseisms with values corresponding to the volume surrounding the hydraulic stimulation.

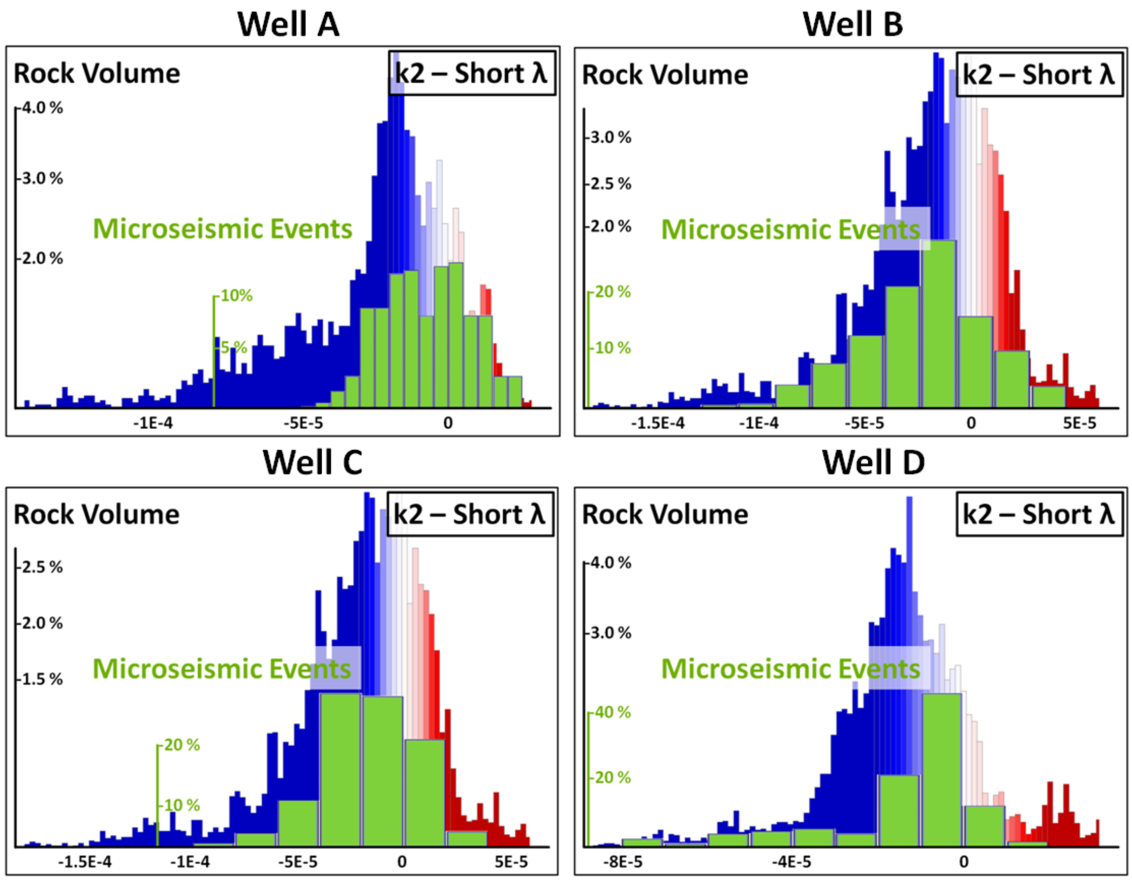

Figure 17. Short wavelength k_2 values of recorded microseisms with values corresponding to the volume surrounding the hydraulic stimulation.

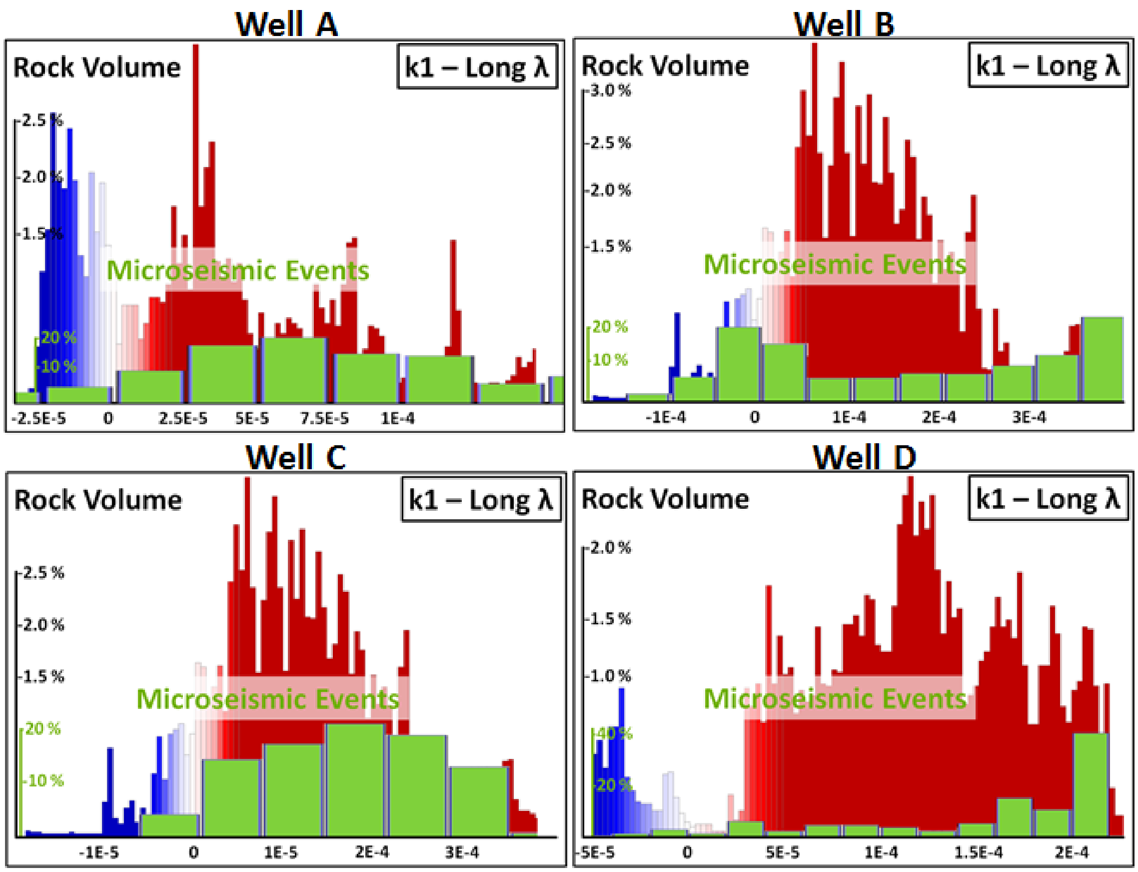

Figure 18. Long wavelength k_1 values of recorded microseisms with values corresponding to the volume surrounding the hydraulic stimulation.

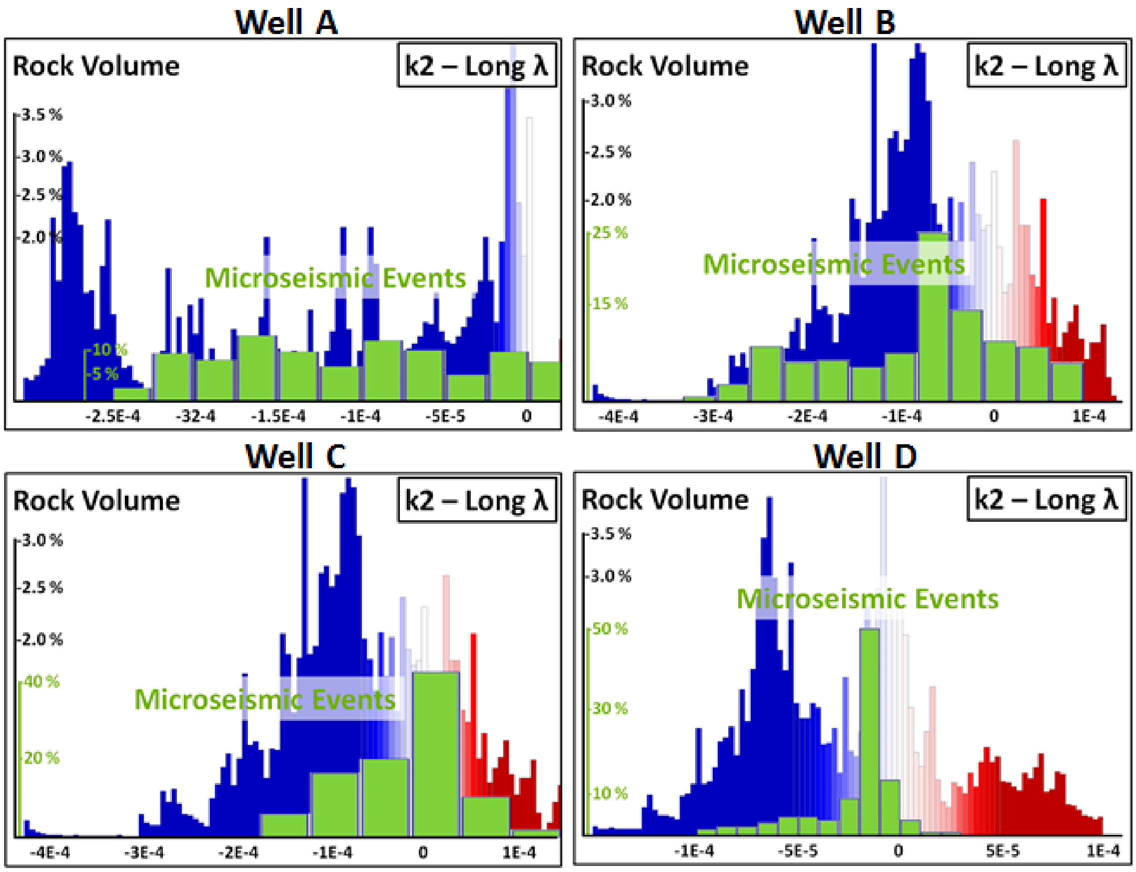

Figure 19. Long wavelength k_2 values of recorded microseisms with values corresponding to the volume surrounding the hydraulic stimulation.

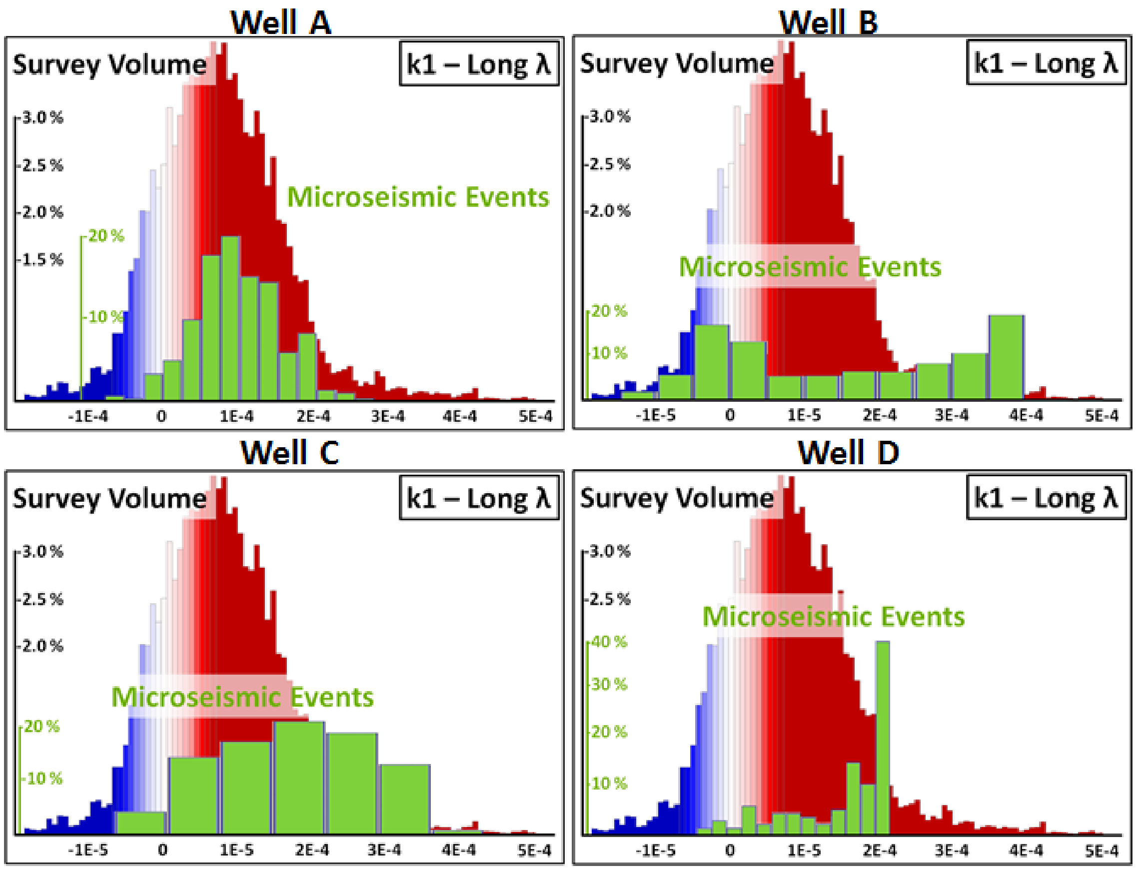

Figure 20. Long wavelength k_1 values of recorded microseisms with values corresponding to the whole seismic volume.

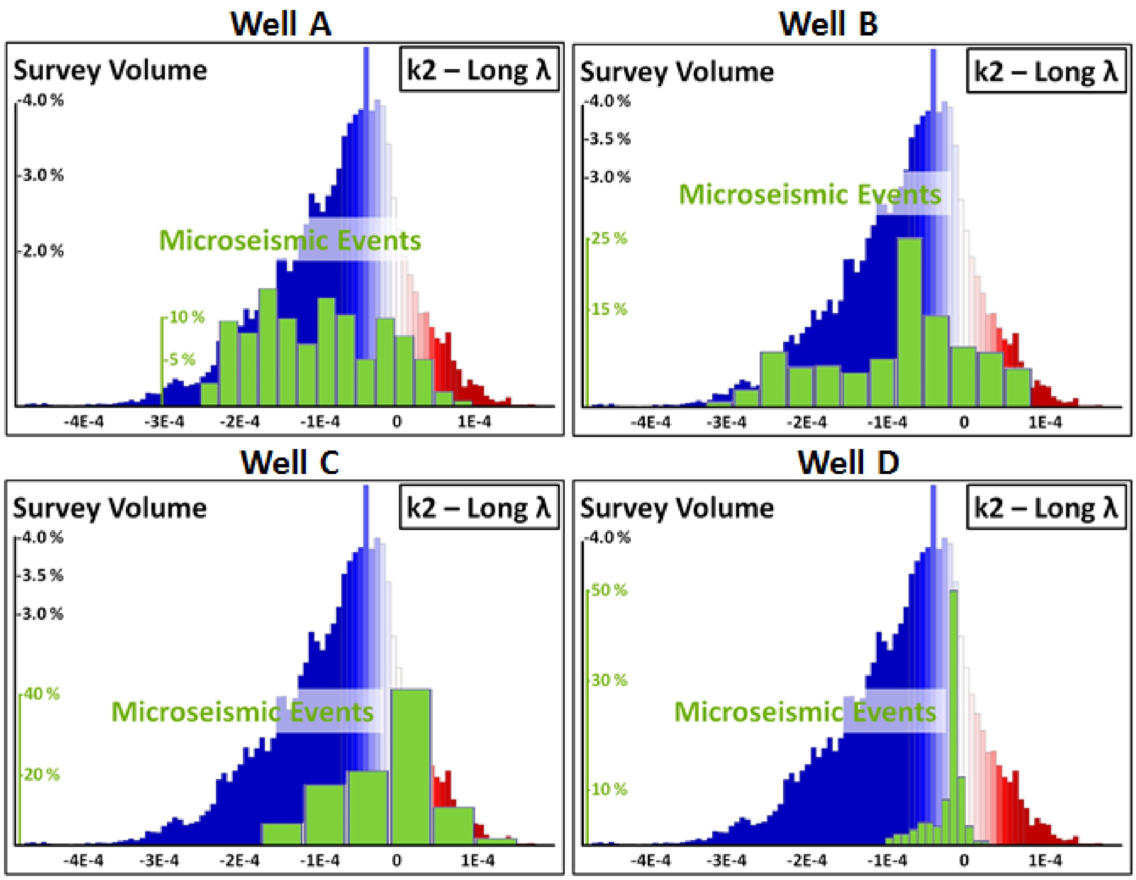

Figure 21. Long wavelength k_2 values of recorded microseisms with values corresponding to the whole seismic volume.

To understand the relationship between the microseisms and curvature values, I analyzed k_1 vs. k_2 plots. As previously mentioned, 3D quadratic shapes can be described using values of k_1 and k_2 (Figure 4). Both short and long wavelength k_1 vs. k_2 plots (Figures 22 and 23) show that the fractured rock is associated with many geologic structures, dominantly ridges, domes and saddles. Although there are a number of events that occur in bowl and valley structures, the majority of the events suggest preferential fracturing of anticlinal structures. I interpret that when local and regional stresses act upon these structures, flexure points weaken, creating potential points of fracture along them. It is possible that preferential fracturing of anticlinal features as opposed to synclinal features can be associated with a difference in deformation at the flexure points from differential stresses or an influence of overburden pressure, although it is unclear.

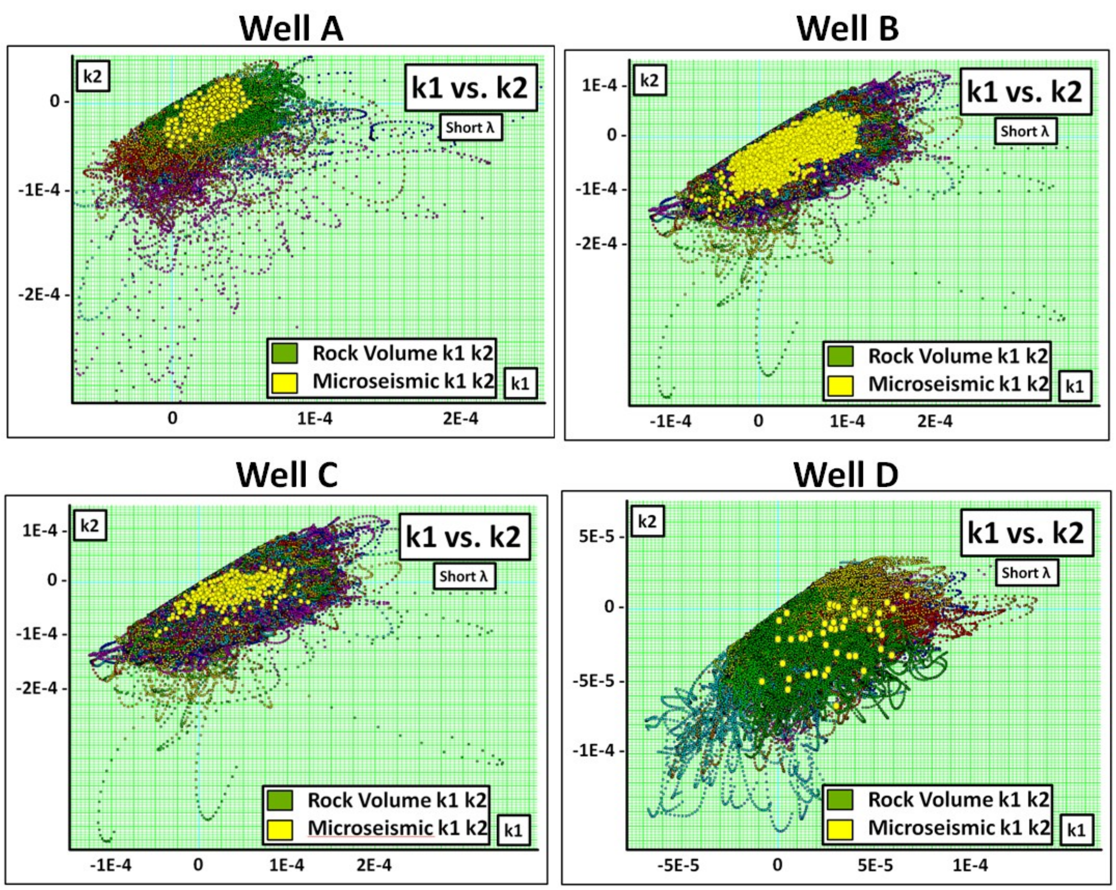

Figure 22. Short wavelength k_1 vs. k_2 cross plots of microseismic event values and the values of the rock volume that surrounds them. Plots show that events occur predominately in ridges and dome structures, even though they also occur in bowl and valley structures.

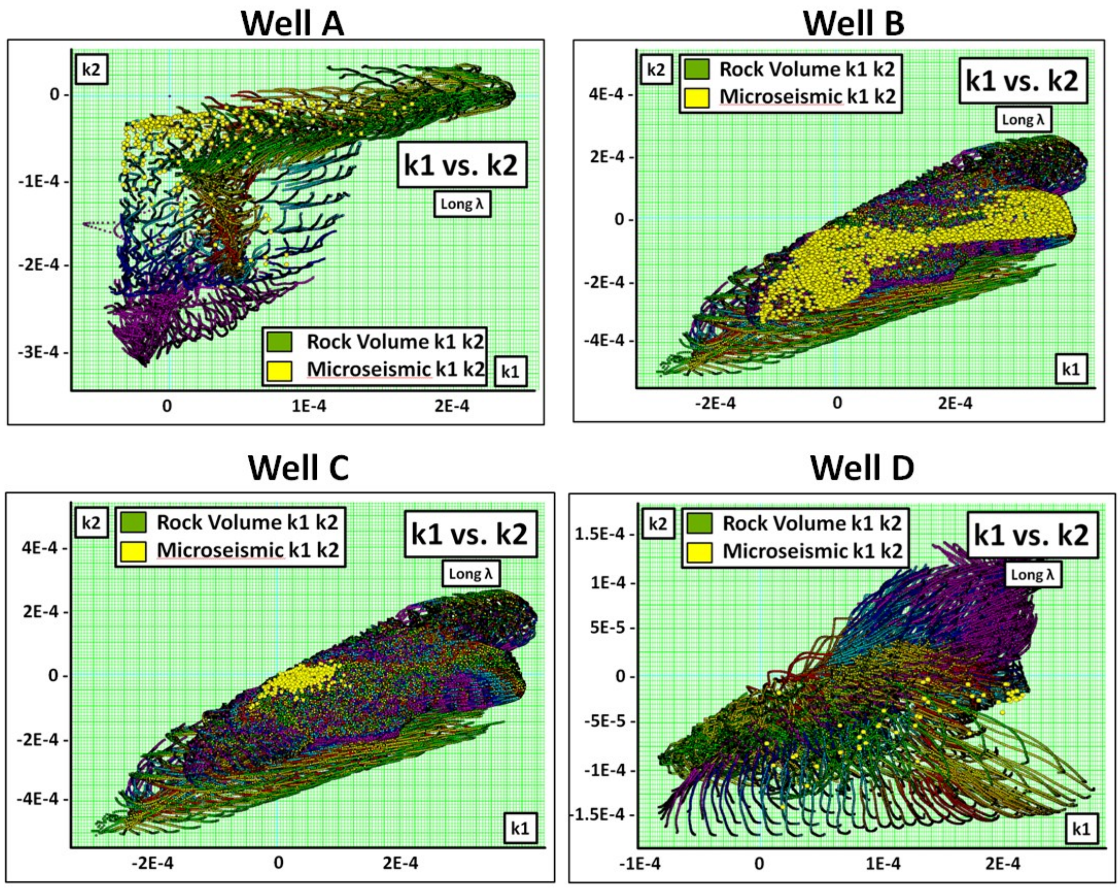

Figure 23. Long wavelength k_1 vs. k_2 cross plots of microseismic event values and the values of the rock volume that surrounds them. Similar to the short wavelength volumetric curvature plots, long wavelength plots show that events occur predominately in ridges and dome structures, even though they also occur in bowl and valley structures.

5.3 Microseisms and Seismic Inversion Properties

By design of the hydraulic fracture job, the microseisms occur primarily within the formation being stimulated, in this case the Lower Barnett Shale. However, the mineralogical composition of the shale is highly variable, resulting in variable fracture gradients and fracture zones (Jarvie et al., 2007). Therefore it is a logical hypothesis that locations of the microseismic events in the Barnett Shale will correlate to the inversion volumes. Indeed, results show that they correspond to a narrow range of inverted values for each property (density, impedance, etc.) in all stimulation stages of the studied wells, regardless of their orientation and location.

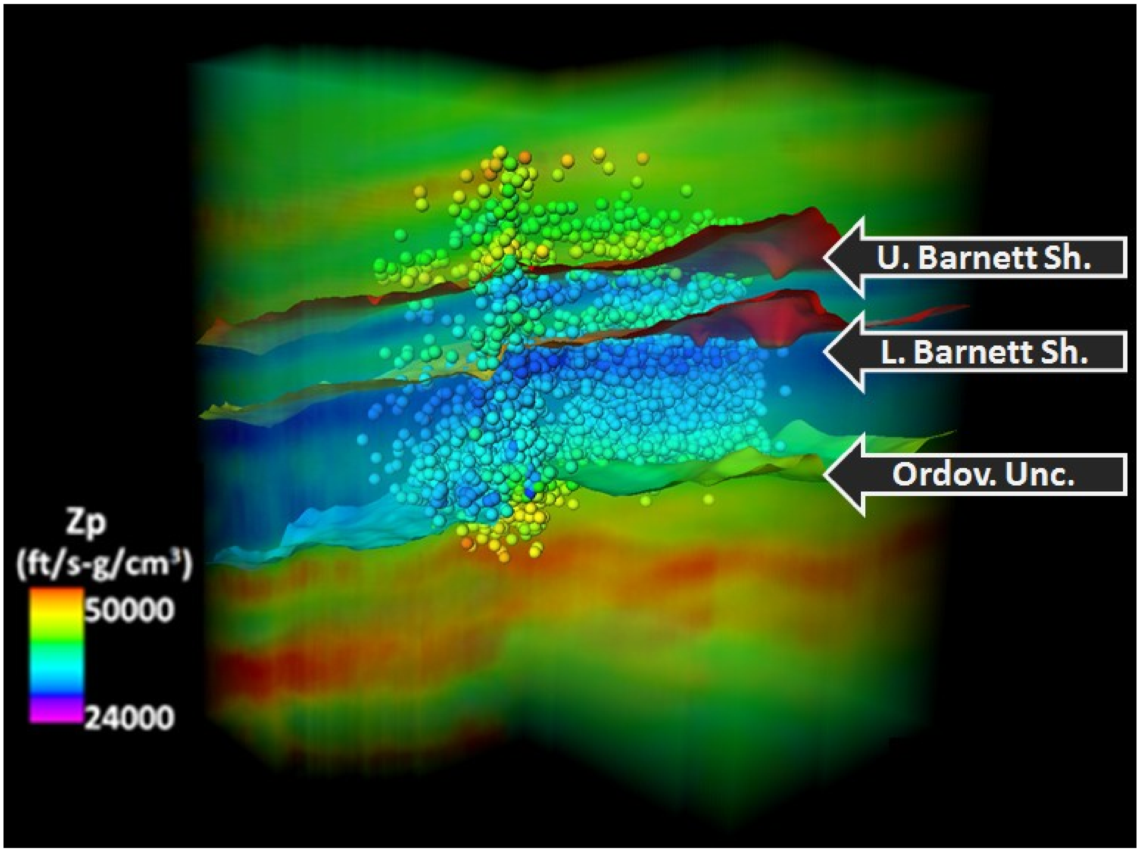

Figure 24. Side-view of microseismic events and surrounding inverted *P*-impedance volume from well *C*. Events have been color-coded with impedance values, mirroring the impedance color ranges from the impedance volume surrounding them. Surfaces help visualize the impedance changes between formations.

Since wells logged before stimulation represent the unfractured medium, and seismic acquired after stimulation images the fractured medium (except in the case of well *A*), certain theoretical modeling errors could be expected in the vicinity of the stimulation wells. It is possible that extensive fracturing could change the medium and lower its density and impedance values from its unfractured state. However, similarities between pre- and post-stimulation seismic imply that any possible change is below the seismic resolution and that both instances can be effectively used for microseismic characterization. Further, the stimulations in this study are limited to only two stages in certain wells, resulting in a modest alteration of the matrix formation. These changes could be observed with a high-density and oversampled surface seismic survey or with core sample testing.

Figure 24 provides a perspective view of the *P*-impedance volume mapped with the well C microseismic event loci. Horizons indicate that most of the events occur within the treated Lower Barnett interval of interest. Figures 25 and 26 show *P*- and *S*-impedance histograms of the microseisms vs. impedance values from the entire volume surrounding the stimulated area. The data suggest that fractures associated with hydraulic stimulation occur in lower impedance rock for all wells.

Furthermore, in wells where stimulation extended beyond the target formation, I find that fractures occur in the lower end of the impedance spectrum corresponding to each formation. For example, while the fractures in well *A* all occurred in the Lower Barnett Shale the stimulation of wells *B* and *C* resulted in fracturing of the overlying Marble Falls Limestone, the target Barnett Shale, and the underlying Ordovician carbonates. Microseisms from wells *B* and *C* mimic the bimodal character of the surrounding rock's values, correlating with the lower values of each mode. Since the fractured rocks have lower impedance and are less dense than the surrounding areas, I interpret preferential fracturing of low velocity zones.

To further investigate impedance values associated with microseisms, I generated *P*-impedance vs. *S*-impedance plots of the stimulated rock near the wells and those at the microseism locations. Figure 27 shows that there is greater occurrence of events for low values of Z_P and Z_S. Furthermore, events show a distinct linear trend corresponding to a

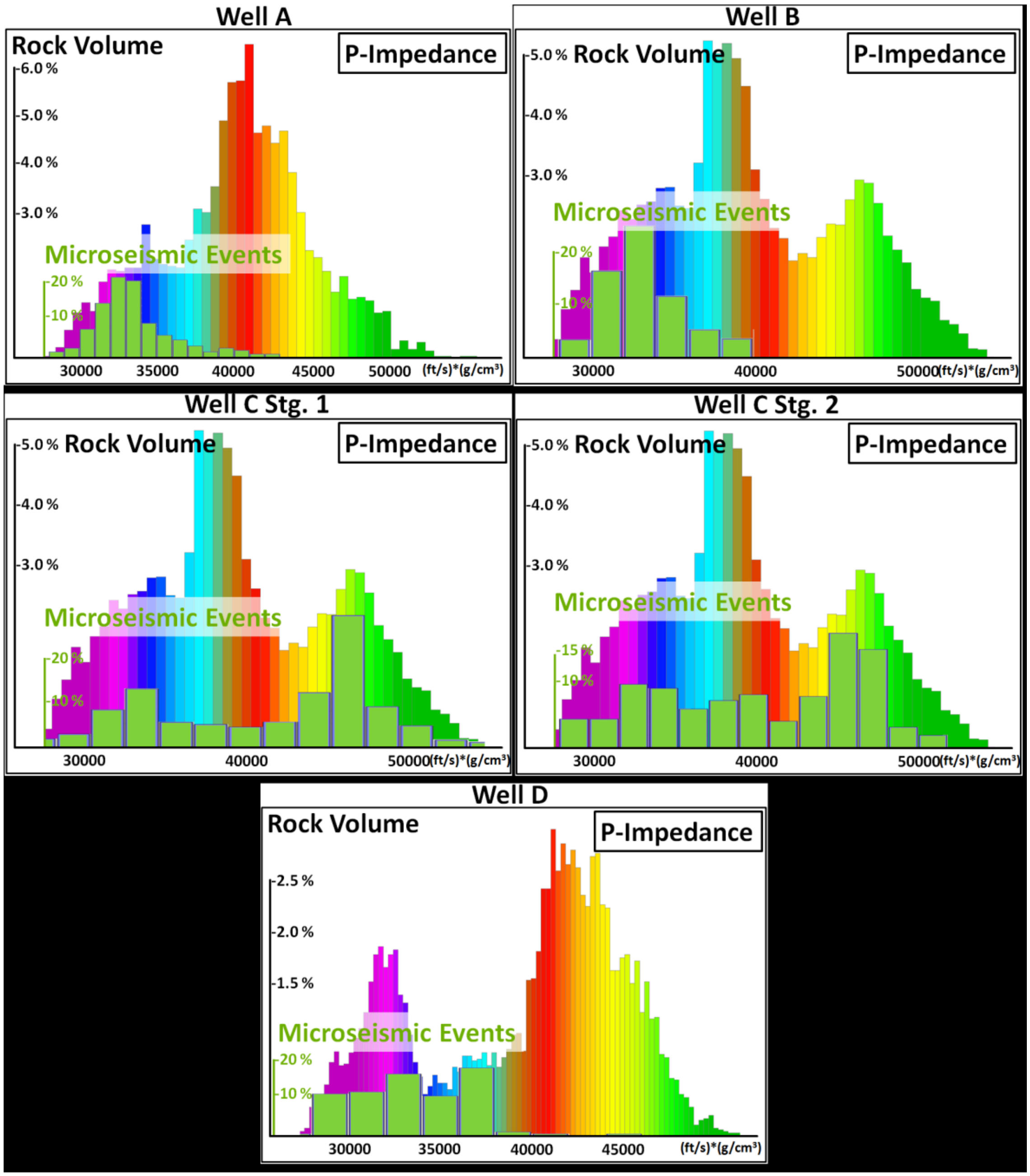

Figure 25. ***P*-impedance values of the rock volume and of stimulated rock volume corresponding to microseismic event locations (in green). Note correlation of event location to lowest values of impedance in wells *A* and *D*. In contrast, wells *B* and *C* exhibit a bimodal behavior with the lower impedance events occurring within the Barnett Shale and higher impedance events in the overlying Marble Falls Limestone and underlying Ordovician carbonates.**

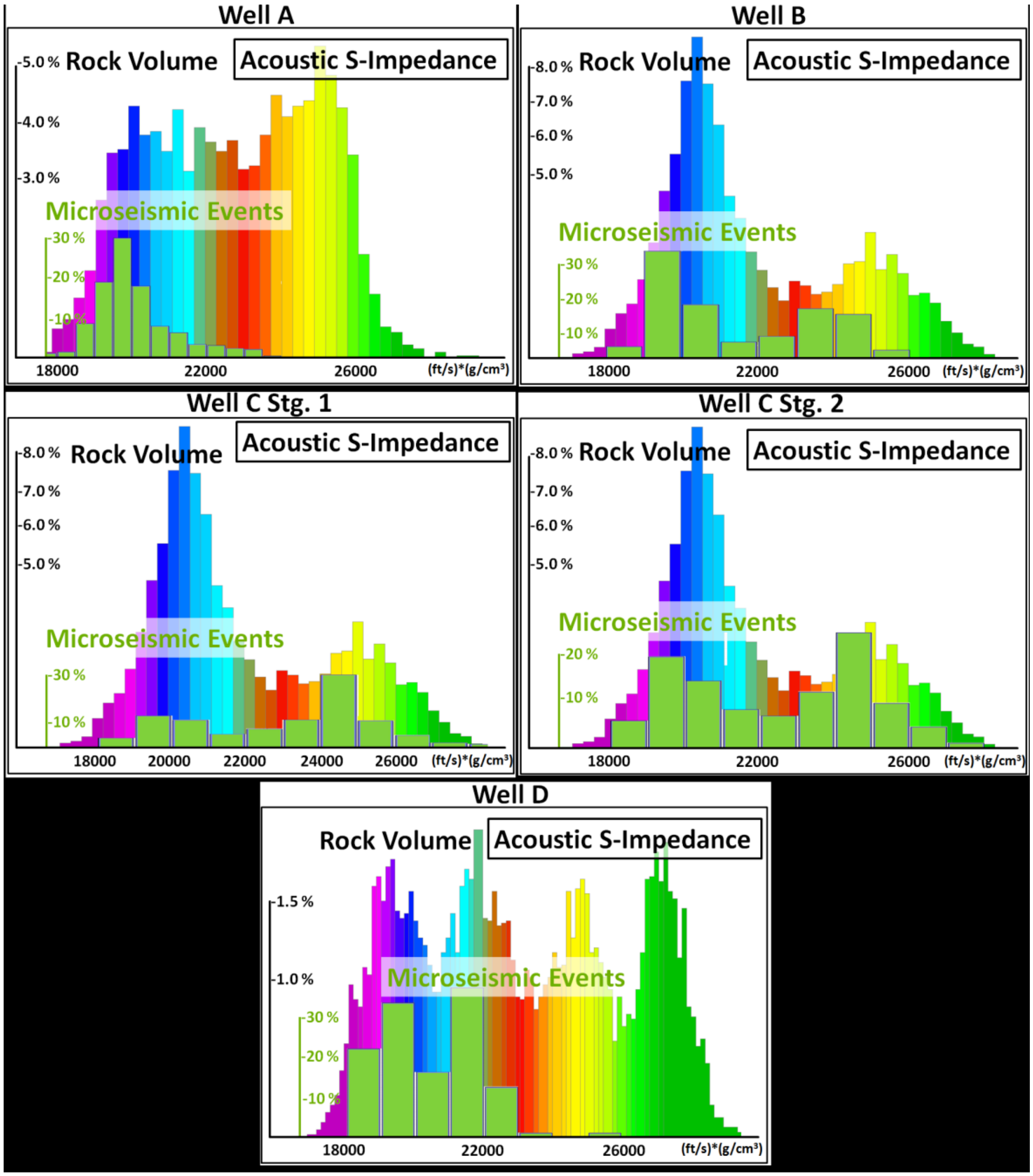

Figure 26. *S*-impedance values of the rock and stimulated volume corresponding to microseismic event locations (in green). Similar to *P*-impedance results, there is a strong correlation of event location to lowest values of impedance in wells *A* and *D*. In contrast, wells *B* and *C* exhibit a bimodal behavior with the lower impedance events occurring within the Barnett Shale and higher impedance events in the overlying Marble Falls Limestone and underlying Ordovician carbonates.

value of $Z_P/Z_S = 1.65$. These crossplots suggest that we can use the inversion of surface seismic data to predict subsurface zones where the rock is more likely to fail and might serve as reservoir drainage pathways.

To further investigate impedance values associated with microseisms, I generated *P*-impedance vs. *S*-impedance plots of the stimulated rock near the wells and those at the microseism locations. Figure 27 shows that there is greater occurrence of events for low values of Z_P and Z_S. Furthermore, events show a distinct linear trend corresponding to a value of $Z_P/Z_S = 1.65$. These crossplots suggest that we can use the inversion of surface seismic data to predict subsurface zones where the rock is more likely to fail and might serve as reservoir drainage pathways.

This microseismic measurement-based analysis indicates that hydraulically-stimulated rocks preferably fail within low impedance zones in all stages of the four fractured wells. This observation is in agreement with those of Rutledge and Phillips' (2003) who also find shear activation of fractures to be correlated to low-impedance. However, this observation contradicts the general assumption that hydraulic stimulation preferentially fractures brittle rock as it generates larger fracture systems and ultimately a more efficient drainage pathway (Grieser et al., 2007; Rickman et al., 2008). To reconcile these conflicting observations, I hypothesize that the low-impedance zones in our survey correspond to lower-impedance, calcite-cemented healed fractures that are more easily propped open than the undisturbed shale. As discussed previously, Gale et al. (2007) found that the tensile strength of the contact between the calcite fracture fill and the shale wall rock is low, leading to a weak fracture-host boundary.

Similar to the impedance results, density histograms show preferential fracturing

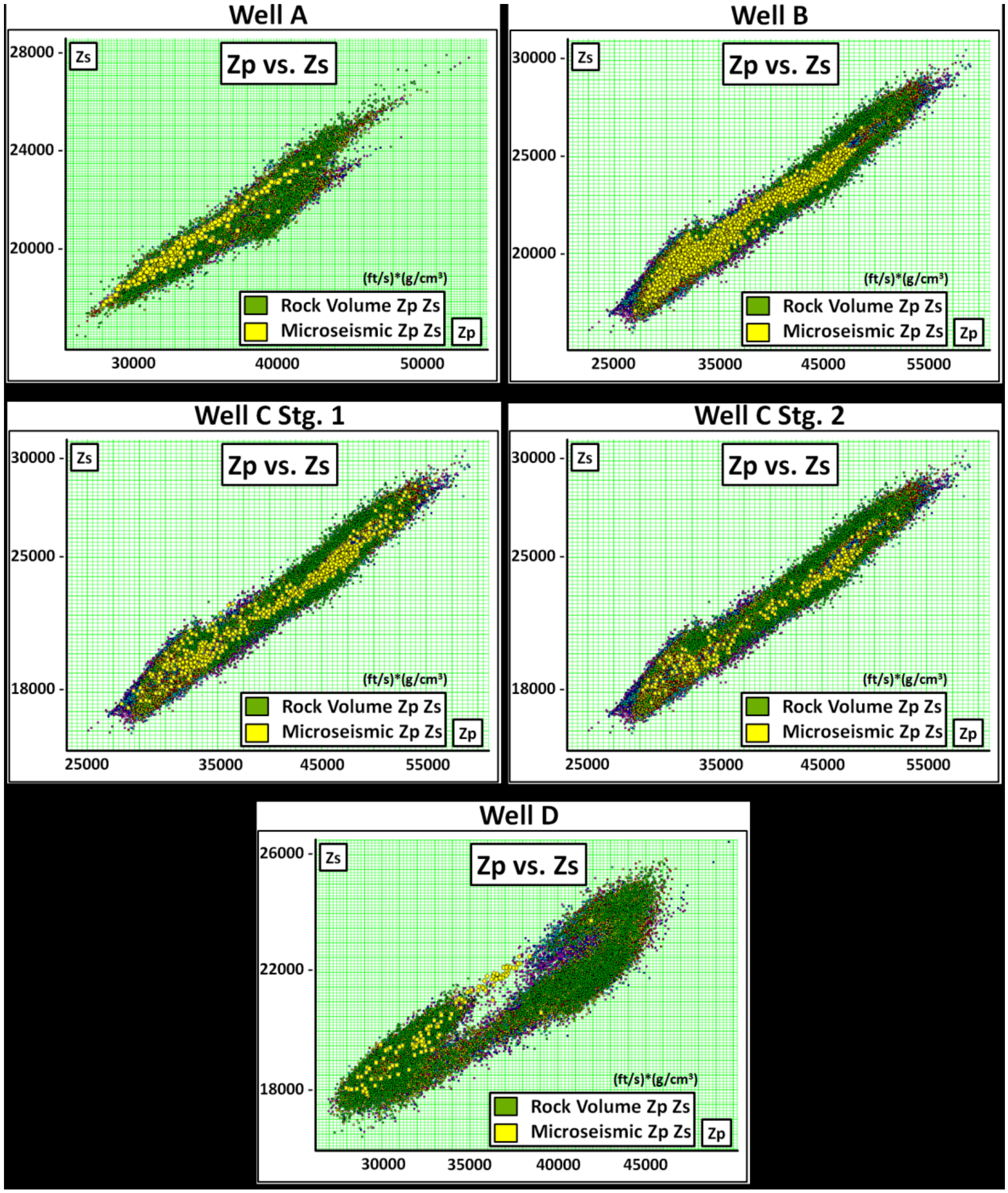

Figure 27. Cross plots of *P*- and *S*-impedance values of the rock volume (in green) and at the microseism event locations (in yellow).

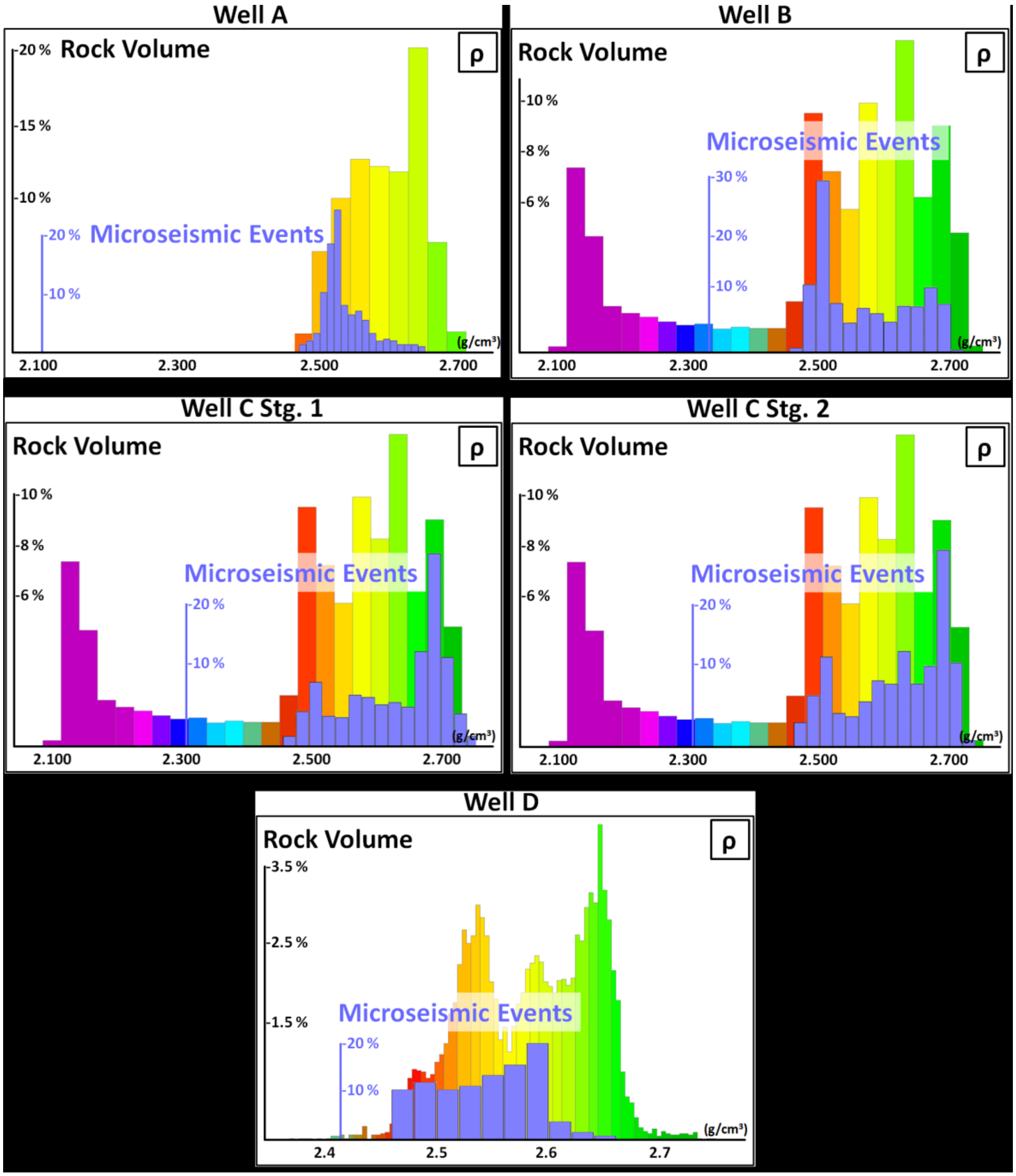

Figure 28. Density of stimulated rock volumes surrounding the hydraulically-stimulated areas and density of mapped microseisms within said volumes. In wells *A* and *D* events with low density correspond to the Barnett Shale. In wells *B* and *C* the bimodal distribution of density values correspond to the low values of the Barnett Shale and the high values of the Marble Falls Limestone and Ordovician carbonates.

towards the lower end of the density spectrum. The observed events occur in the less dense areas of the Barnett Shale (Figure 28). This also applies to wells *B* and *C*, where hydraulic fractures "leak" into other formations. Taking into account the low impedance and low density character of the microseism-generating zones, the modulus could have high velocities. It is possible that while events might be occurring in higher density rock, they might have an asesimic behavior, or generate non-recordable energy.

Lamé parameters λ and μ (incompressibility and rigidity), are a function of the acoustic and shear impedances, Z_p and Z_s, and density, ρ.

$$\lambda\rho = Z_p^2 - 2Z_s^2 \text{, and} \tag{12}$$

$$\mu\rho = Z_s^2. \tag{13}$$

These parameters are used to improve delineation of reservoirs because incompressibility is sensitive to both the pore fluids and the matrix, whereas the rigidity is influenced by the matrix only (Dufour et al., 2002). In Figure 29 I examine the relationship between Lamé parameters of microseism event location to the $\lambda\rho$ and $\mu\rho$ values of the surrounding rock.

Low incompressibility and rigidity values in well *A* and *D* correspond to those of the Barnett Shale. In well *B* and C where the stimulation reaches the Marble Falls Limestone and Ordovician carbonates, we observe a bimodal behavior of the histogram, with the lowest mode corresponding to Barnett Shale values and the highest mode corresponding to carbonate values. The fractured $\lambda\rho$ and $\mu\rho$ zones are in the lowest values of the Barnett Shale mode and in the highest values of the Ordovician Carbonates mode (Figure 29).

In Figure 30 I display a cross plot of $\lambda\rho$ vs. $\mu\rho$ in the surrounding rock (in green) and values at the microseism event locations (in yellow). I note a linear trend of the microseismic points, breaking into two subclusters, indicating the fractures in both the Barnett Shale and the Ordovician Carbonates.

Goodway et al. (2006) concluded from a conventional isotropic AVO study of the Barnett Shale that the optimum gas shale properties have relatively low incompressibility (λ) and high rigidity (μ), setting the optimum scenario for supporting extensive induced fractures. They state that these properties also produce the lowest closure stresses, or largest fractures. Rigidity (μ) determines the resistance to shear failure and incompressibility (λ) is the resistance to fracture dilation, which is related to pore-pressure (Figure 31).

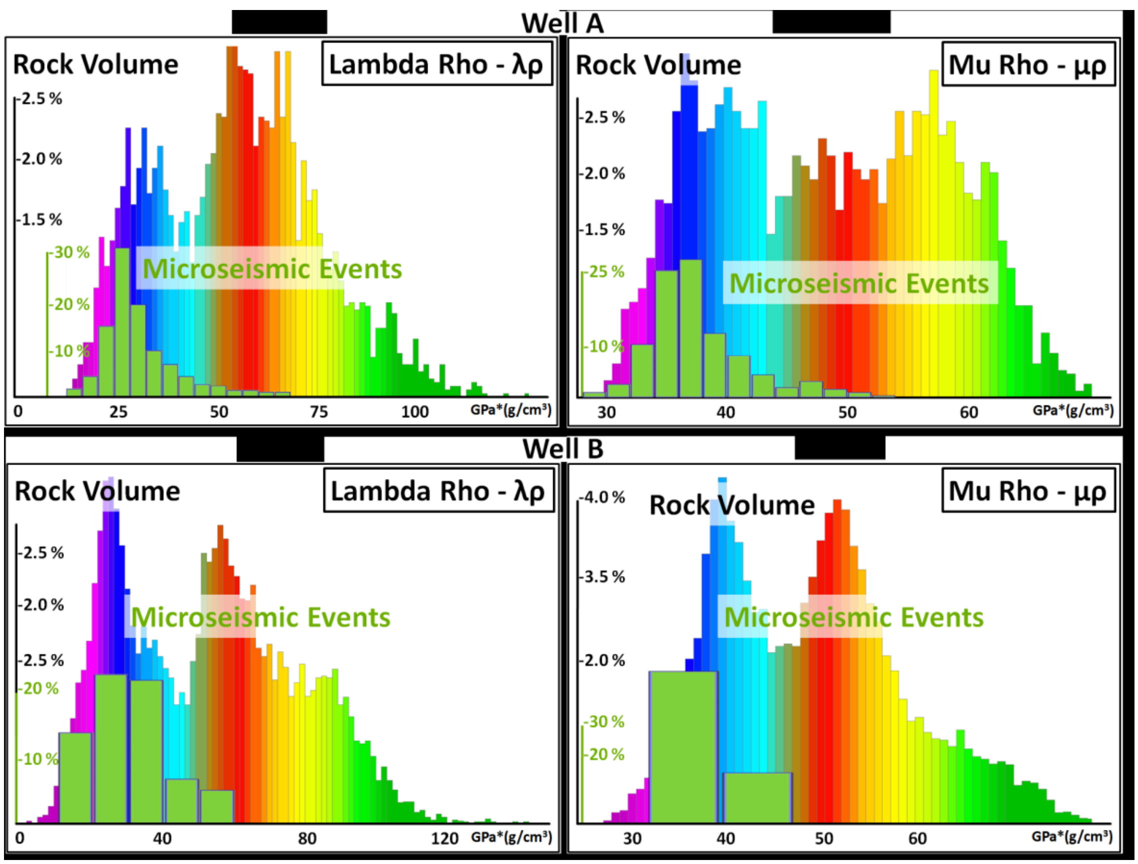

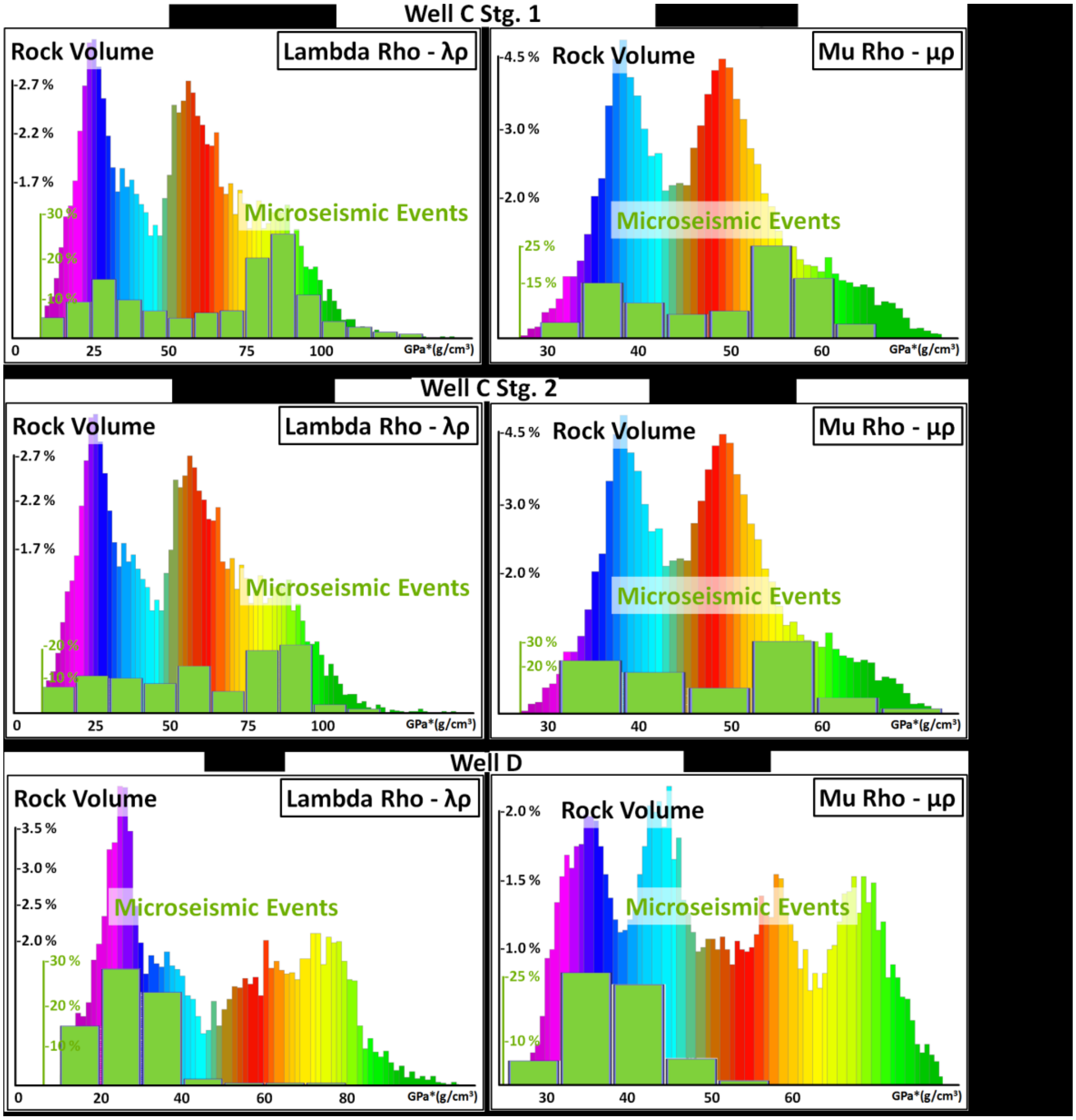

Figure 29. Histograms of microseismic $\lambda\rho$ and $\mu\rho$ values compared to those of the surrounding volume of rock. In wells *A* and *D* events with low rigidity and incompressibility correspond to the Barnett Shale. In wells *B* and *C* the bimodal distribution of microseismic rigidity and incompressibility values correspond to the low values of the Barnett Shale and the high values of Ordovician carbonates.

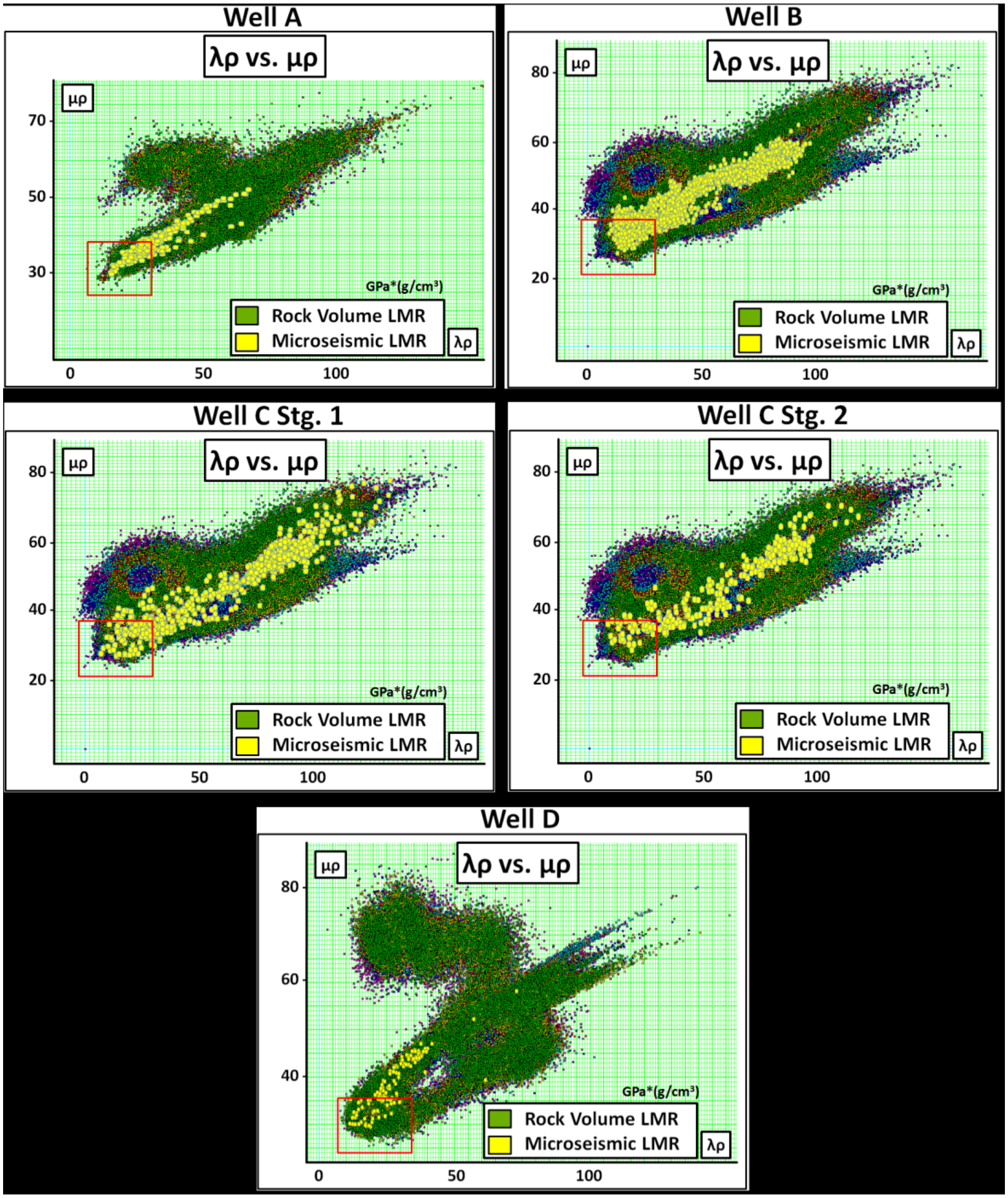

Figure 30. Cross plots of $\lambda\rho$ and $\mu\rho$ values of the rock volume (in green) and at the microseism event locations (in yellow). Fractured rock corresponds to a semi-linear trend similar to that of the *P*- and *S*- impedance cross plots. Red squares define the potential gas-rich zones corresponding to low $\lambda\rho$ and $\mu\rho$ values as defined by Aibaidula and McMechan (2009).

Figure 31. Rigidity and incompressibility as they relate to fracture shear failure and dilatation and horizontal stress directions (from Goodway et al., 2006).

To evaluate well placement and stimulation effectiveness with respect to the assumed gas-rich areas, I used map views from Figure 10 with the mapped microseisms (Figure 32). Pseudo-logs extracted from the inverted volumes along the wellbore were placed for reference, and time slices at the level of the horizontal portion of the well show lateral changes of the properties. By design, the induced hydraulic fractures propagate predominately along the gas bearing Barnett Shale. Gas saturated V_p/V_s ratios are assumed to be between 1.84 to 1.99 for limestone, 1.7 to 3.0 for shale (Aibaidula and McMechan, 2009), and for $\lambda\rho$ values that are less than $\mu\rho$ (Goodway et al., 2006). Using these assumptions, Wells *B* and *C* show values that match gas saturated areas, with V_p/V_s ratios of approximately 1.8 and $\lambda\rho$ being less than $\mu\rho$. This explains higher production history of wells *B* and *C* than wells *A* and *D*. Conversely, well *A* shows V_p/V_s ratios of approximately 1.7 and $\lambda\rho$ greater than $\mu\rho$, correlating to the well's low production. Well *D* shows very similar characteristics but has a production history comparable to wells *B* and *C*. Closer study of this well reveals the vertical extent of the microseisms into zones with characteristics of gas saturated rocks, in spite of the limited lateral extent of the induced fracture system. Figure 33 illustrates the interaction of induced fracture systems from adjacent stimulating wells *B* and *C* in the Lower Barnett Shale. It should be noted that the effectiveness of stimulation can vary depending on the viscosity of the stimulation fluid, the pressure applied, and the duration of each stimulation stage. Stimulation details were unknown at the time of this investigation.

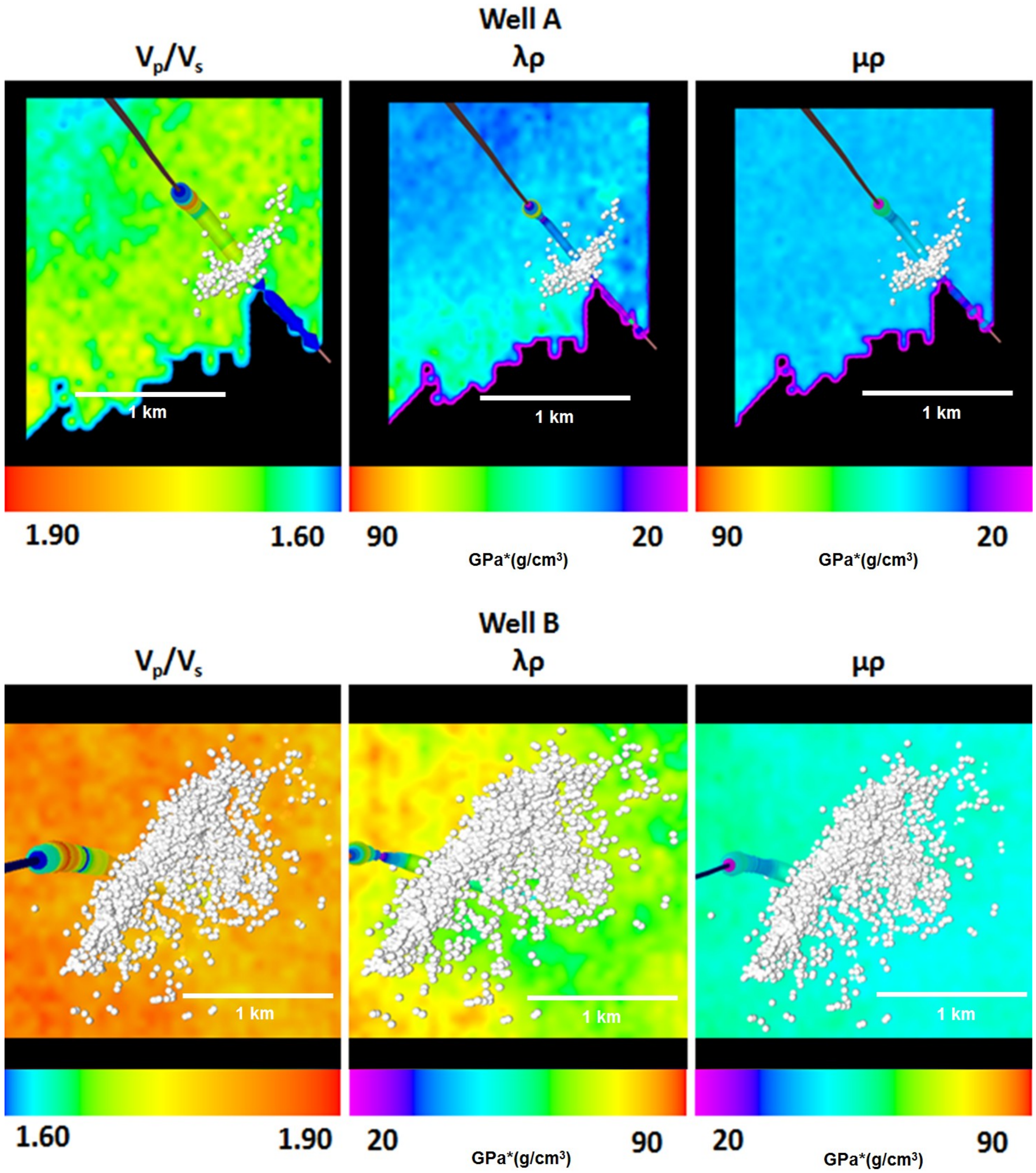

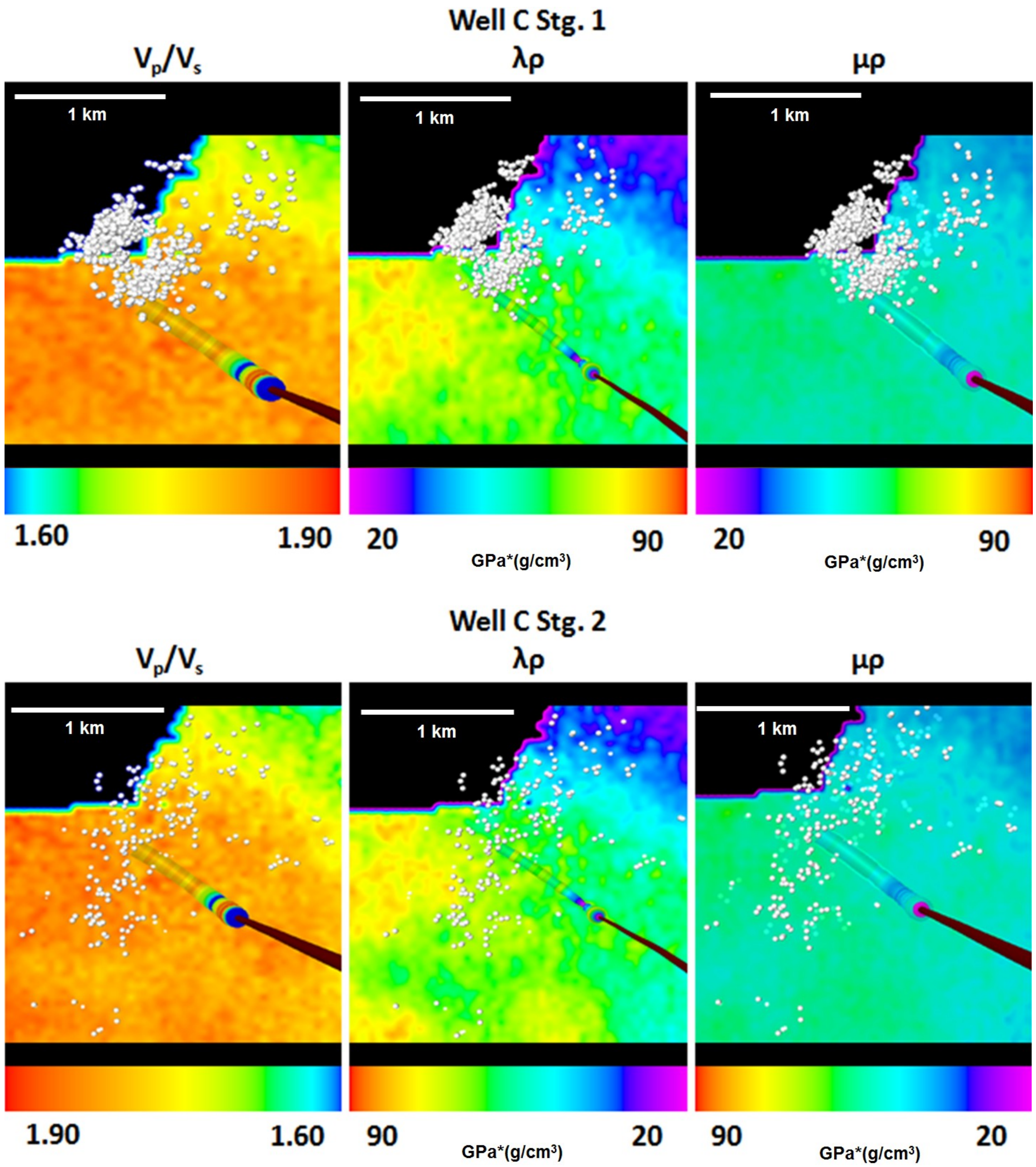

Well C Stg. 1
Vp/Vs
λρ
μρ
1 km
1 km
1 km
1.60
1.90
20
GPa*(g/cm3)
90
20
GPa*(g/cm3)
90
Well C Stg. 2
Vp/Vs
λρ
μρ
1 km
1 km
1 km
1.90
1.60
90
GPa*(g/cm3)
20
90
GPa*(g/cm3)
20

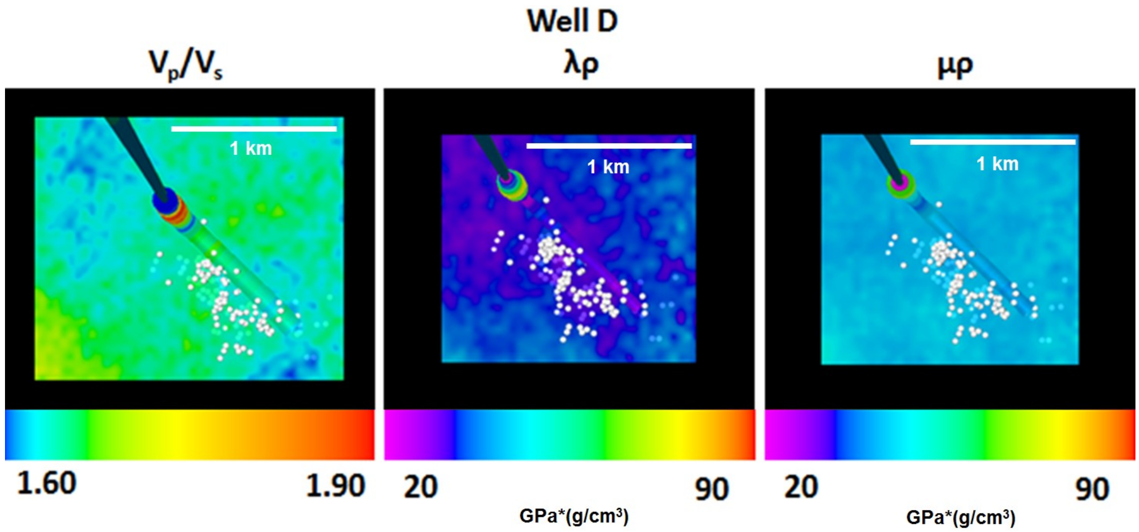

Figure 32. Map view of mapped microseisms with time slices of *Vp*/*Vs* ratio and LMR values across the horizontal portion of stimulation wells, with pseudlo-logs extracted from the corresponding volumes along the length of the wellbores. Wells *A* and *D* show fracture systems with relatively low lateral extent, compared to wells *B* and *C*.

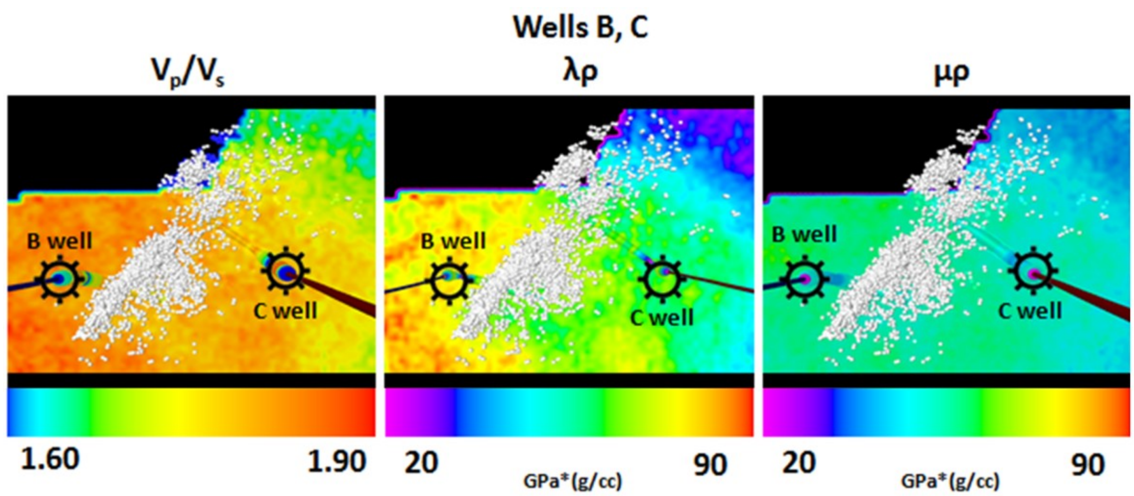

Figure 33. Map view of mapped microseisms from wells *B* and *C* with time slices of *Vp*/*Vs* ratio and LMR values across the horizontal portion of stimulation wells, with pseudlo-logs extracted from the corresponding volumes along the length of the wellbores.

6. CONCLUSIONS

Shale gas is currently the fastest growing hydrocarbon resource play in North America. Since shales have extremely low permeability, the shale needs to be hydraulically fractured in order to produce hydrocarbons. The cost of drilling and hydraulic fracturing is very high, with hundreds of wells needed to produce a small field area. Not surprisingly, there are good wells and mediocre wells. The goal of this thesis was to evaluate the use of 3D surface seismic data in predicting the behavior of a well before it is drilled and hydraulically fractured

I predict fracture-prone zones in the subsurface from pre-stack *P*- and *S*-impedance inversion of surface seismic data calibrated to microseismic event locations. Coupling this method with the positive correlation of induced fractures and curvature anomalies, I suggest a workflow that provides *a priori* knowledge of potential fracture system distribution. The correlation of microseisms with surface seismic inversion and curvature attributes can be used for improved stimulation plans. Knowledge of possible drainage pathways that lead to target zones can ultimately increase recovery rates from hydraulic stimulation.

Microseismic events associated with hydraulic fracturing are directly correlated to the regional stress patterns, mimicking primary and secondary faults. Formation contact zones were found to act as a relatively impermeable barrier for propagating fracture systems and also act as weakness planes. Hydraulic fractures tend to fracture rock predominately along most positive principal volumetric curvature zones, while avoiding most negative principal curvature areas. These fractures correlate to anticlinal 3D shapes like ridges, domes, and saddles.

Pre-stack inversion of density, and *P*- and *S*-impedance, shows that microseisms fracture low-density and low-impedance rock. It is likely that the failure of low density and low impedance rocks is associated with the flow of stimulation fluids through weak calcite-cemented fractures and faults as paths of least resistance.
delineate the extent of the fracture systems into gas-bearing zones and the effectiveness of the hydraulic stimulation project through production.

7. RECOMMENDATIONS

Several recommendations can be made from the procedures and conclusions of this investigation. The accuracy of our inversion volume could be increased significantly with the use of a fully processed pre-stack migrated seismic dataset. This would generate more precise *P*- and *S*-impedance, V_p/V_s ratio and Lamé parameters volumes and the microseism values associated with them. Similarly, processing of the raw microseismic data, rather than using processed data, would provide information on parameters including source mechanism, noise, energy, anisotropy, and location error. The combination of these factors will allow for a better assessment of the datasets as well as uncertainties in the data and derivative products.

Time dependency of the microseisms and its association with seismic attributes and inverted volumes would help characterize which parameters govern induced fracture system propagation. An understanding of production rate changes before and after hydraulic fracturing will show the effectiveness of the stimulation projects in generating fracture systems that extend along gas bearing zones.

REFERENCES

Aibaidula, A., and G. McMechan, 2009, Inversion and interpretation of a 3D seismic data set from the Ouachita Mountains, Oklahoma: Geophysics, **74**, B37-B45.

Al-Dossary, S., and K. J. Marfurt, 2006, 3D volumetric multispectral estimates of reflector curvature and rotation: Geophysics, **71**, 41–51

Blumentritt, C. H., K. J. Marfurt, and E. C. Sullivan, 2006, Volume-based curvature computations illuminate fracture orientations – Early to mid-Paleozoic, Central Basin Platform, west Texas: Geophysics, **71**, B159-B166.

Chopra, S., and K. J. Marfurt, 2007, Volumetric curvature attributes add value to 3D seismic data interpretation: The Leading Edge, **26**, 856-867.

Chopra, S., and D. Pruden, 2003, Multiattribute seismic analysis on AVO-derived parameters - A case study: The Leading Edge, **10,** 998-1002.

Daniels J., G. Waters, J. Le Calvez, J. Lassek, and D. Bentley, 2007, Contacting More of the Barnett Shale Through an Integration of Real-Time Microseismic Monitoring, Petrophysics, and Hydraulic Fracture Design: Society of Petroleum Engineers Annual Technical Conference and Exhibition, 110562-MS.

Dufour, J., J. Squires, W. N. Goodway, A. Edmunds, and I. Shook, 2002, Integrated geological and geophysical interpretation case study, and Lamé rock parameter extractions using AVO analysis on the Blackfoot 3C-3D seismic data, southern Alberta, Canada: Geophysics, **67**, 27-37.

Dvorkin, J., G. Mavko, and A. Nur, 1999, Overpressure detection from compressional- and shear-wave data: Geophysical Research Letters, 3417-3420.

Gale, J. F., R. M. Reed, and J. Holder, 2007, Natural fractures in the Barnett Shale and their Importance for hydraulic fracture treatments: AAPG Bulletin, **91**, 603-622.

Goffey, R., 2009, AVO, inversion or AVO inversion? Hampson-Russell's software solutions: O&G Next Generation e-magazine, **9**. Accessed July 2010.

Goodway, B., T. Chen, and J., Downton, 1997, Improved AVO fluid detection and lithology discrimination using Lamé petrophysical parameters; "λρ","μρ",&"λ/μ fluid stack", from P and S inversions: 67th Annual International Meeting, SEG, Expanded Abstracts, 183-186.

Grieser, B., and J. Bray, 2007, Identification of production potential in unconventional reservoirs: Presented at the Production and Operations Symposium, Society of Petroleum Engineers.

Hampson, D. P., and B. H. Russell, 2005, Simultaneous inversion of pre-stack seismic data: 75th Annual International Meeting, SEG, Expanded Abstracts, 1633-1637.

Jarvie, D. M., R. J. Hill, T. E. Ruble, and R. M. Pollastro, 2007, Unconventional shale-gas systems: The Mississippian Barnett Shale of north-central Texas as one model for thermogenic shale-gas assessment: AAPG Bulletin, **91**, 475-499.

Kidney, R. L., U. Zimmer, and N. Boroumand, 2010, Impact of distance-dependent location dispersion error on interpretation of microseismic event distributions: The Leading Edge, **29**, 284-289.

Lakings, J. D., P. M. Duncan, and C. Neale, 2006, Surface based microseismic monitoring of a hydraulic fracture well stimulation in the Barnett Shale: 76th Annual International Meeting, SEG, Expanded Abstracts, 605-608.

Le Calvez, J. H., L. Bennett, K. V. Tanner, W. D. Grant, L. Nutt, V. Jochen, W. Underhill, and J. Drew, 2005, Monitoring microseismic fracture development to optimize stimulation and production in aging fields: The Leading Edge, **24**, 72-75.

Lisle, R. J., 1994, Detection of zones of abnormal strains in structures using Gaussian curvature analysis: AAPG Bulletin, **78**, 1811-1819.

Loucks, R. and S.T. Ruppel, 2007, Mississippian Barnett Shale: Lithofacies and depositional setting of a deep-water shale-gas succession in the Fort Worth Basin, Texas: AAPG Bulletin, **91**, 579-601.

Mai, H. T., 2010, Seismic attribute analysis and its application to mapping folds and fractures: Diss. University of Oklahoma.

Mai, H. T., K. J. Marfurt, and S. Chávez-Pérez, 2009, Coherence and volumetric curvatures and their spatial relationship to faults and folds, an example from Chicontepec basin, Mexico: 79th Annual International Meeti

Martineau, D. F., 2007, History of the Newark East field and the Barnett Shale as a gas reservoir: AAPG Bulletin, **91**, 399-403.

Masaferro, J. L., M. Bulnes, J. Poblet, and M. Casson, 2003, Kinematic evolution and fracture prediction of the Valle Morado structure inferred from 3-D seismic data, Salta Province, northwest Argentina: AAPG Bulletin, **87**, 1083-1104.

Miskimins, J., 2009, The importance of geophysical and petrophysical data integration for the hydraulic fracturing of unconventional reservoirs: The Leading Edge, **28**, 844-849.

Nelson, R. A., 2001, Geologic analysis of naturally fractured reservoirs: Gulf Professional Publishing, 2nd edition, Houston, TX.

Pollastro, R. M., D. M. Jarvie, R. J. Hill, and C.W. Adams, 2007, Geologic frameqork of the Mississippian Barnett Shale, Barnet-Paleozoic total petroleum system, Bend arch-Fort Worth Basin, Texas: AAPG Bulletin, **91**, 405-436.

Rich, J. P. and M. Ammerman, 2010, Unconventional Geophysics for Unconventional Plays: Presented at the SPE Unconventional Gas Conference, Society of Petroleum Engineers, 131779-MS.

Rickman, R., M. Mullen, E. Petre, B. Grieser, and D. Kundert, 2008, A practical use of shale petrophysics for stimulation design optimization: Presented at the 2008 Society of Petroleum Engineers Annual Technical Conference and Exhibition.

Roberts, A., 2001, Curvature attributes and their applications to 3D interpreted horizons: First Break, **19**, 85-100.

Rothert, E., and S. A. Shapiro, 2003, Microseismic monitoring of borehole fluid injections: Data modeling and inversion for hydraulic properties of rocks: Geophysics, vol. **68**, 685-689.

Rutledge, J. T., and W. S. Phillips, 2003, Hydraulic stimulation of natural fractures as revealed by induced microearthquakes, Carthage Cotton Valley gas field, east Texas: Geophysics, **68**, 441-452.

Vanorio, T., and G. Mavko, 2006, Vp/Vs ratio in gas-pressured saturated sandstones: 76th Annual International Meeting, SEG, Expanded Abstracts, 1545-1549.

Warpinski, N., 2009, Microseismic Monitoring: Inside and out; JPT, **11**, 80-85.